

AD-A053 073

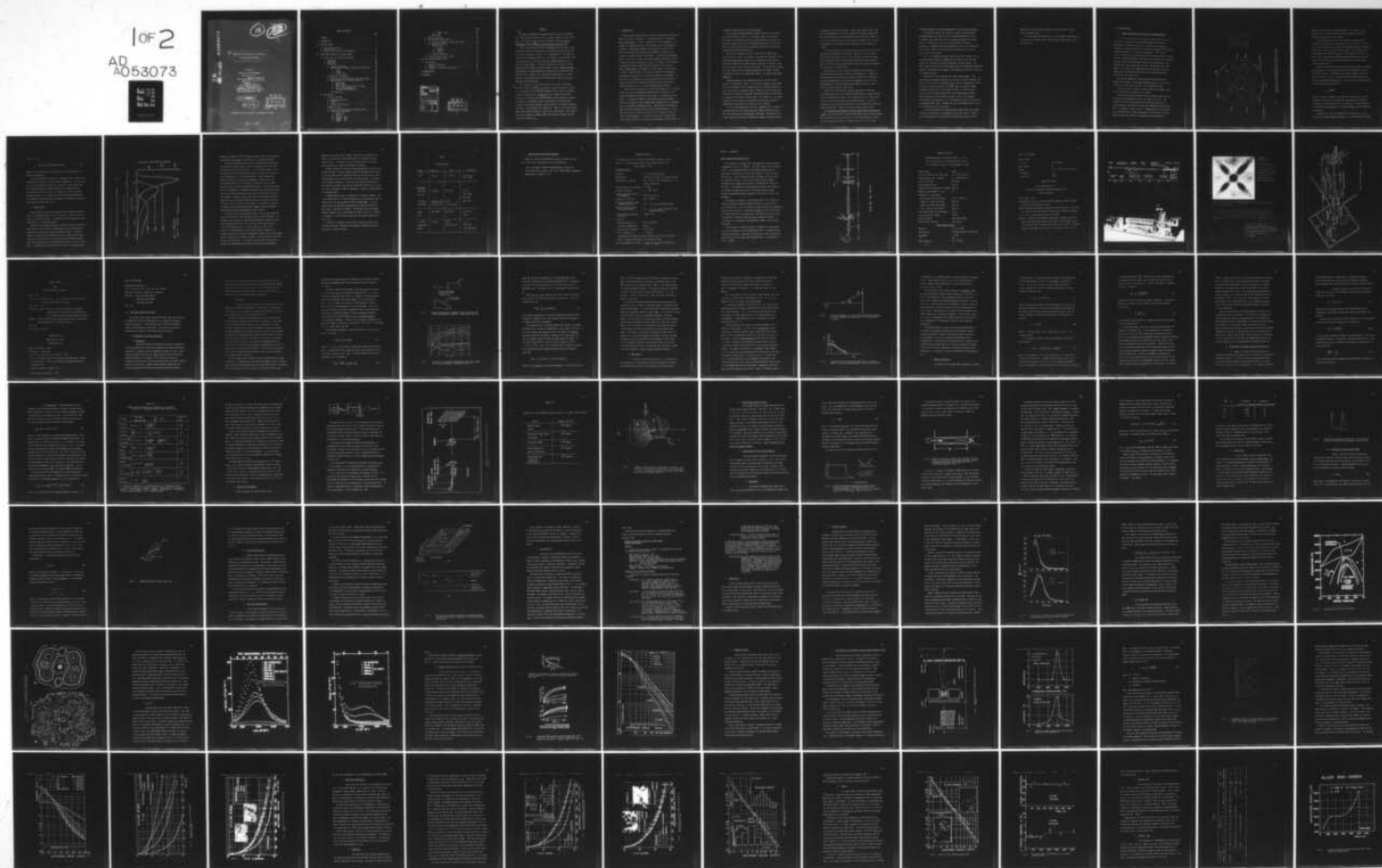
STATE UNIV OF NEW YORK AT STONY BROOK DEPT OF MATERIA--ETC F/6 14/2
NON-DESTRUCTIVE EVALUATION OF MATERIALS WITH COLD NEUTRON BEAMS--ETC(U)
DEC 77 H HERMAN

N00019-77-M-0418

UNCLASSIFIED

NL

1 of 2
AD
A053073



AD No.

ADA 053073

DDC FILE COPY

10

~~10~~

6

NON-DESTRUCTIVE EVALUATION OF MATERIALS
WITH COLD NEUTRON BEAMS,

A Report to
NAVAL AIR SYSTEMS COMMAND ✓
Washington, D.C.

Contract No. N00019-77-M-0418^{new}

15 by
10

Professor Herbert/Herman
Department of Materials Science,
State University of New York at
Stony Brook, New York 11794

11 Dec 1977

13 164 p.

DDC
RECEIVED
APR 24 1978
D

APPROVED FOR PUBLIC RELEASE; DISTRIBUTION UNLIMITED

401 074

mt

TABLE OF CONTENTS

	Page
SYNOPSIS	1
I INTRODUCTION	2
II NEUTRON SOURCES.	7
A. Steady State Reactors.	7
B. Other Sources.	9
C. Reactors with SANS and Cold Neutrons	13
III SMALL-ANGLE NEUTRON SCATTERING (SANS).	20
A. Interactions of Neutrons with Matter	20
1. Absorption	20
2. Scattering	21
3. SANS Theory.	24
a. Radius of Gyration	26
b. Determination of Shape, Volume and Surface Area.	29
i. Shape.	29
ii. Volume	30
iii. Surface Area	31
4. Experimental Arrangements.	33
a. Double-Bragg Scattering-Cold Source Requirement.	36
b. Monochromators for Low-Energy Neutrons	36
i. Guide Tubes.	36
ii. Beam Filters	41
iii. Mechanical Velocity Selectors (MVS).	42
iv. Crystal Monochromators	44
v. Multilayer Monochromators.	44
c. Area Detectors	46
B. Applications	48
1. Thermal Treatments	49
a. Amorphous $\text{SiO}_2\text{-Al}_2\text{O}_3$	51
b. Pt-40% Au.	51
c. Fe-Cr.	53
d. Avional (Al-base Cu-Si).	54
2. Commercial Alloys.	55
a. Precipitation Strengthened Stainless Steels.	56
b. Nickel-Base Superalloys.	59
i. UDIMET-710	59
ii. IN-100	61
iii. INCOLOY - 800.	62
iv. INCOLOY - 700.	62
v. INCONEL - 750.	64

	Page
vi. UDIMET - 520.	66
c. ARMCO IRON.	67
3. Radiation Effects	68
4. Miscellaneous Applications.	72
a. Plastic Deformation, Fatigue and Creep.	73
b. Hydrogen in Metals.	76
c. Porous Solids	77
i. Ceramics.	77
ii. Coatings.	77
iii. Cement.	77
d. Composite Materials	79
5. Review of Applications of SANS.	79
IV COLD NEUTRON RADIOGRAPHY (CNR).	81
A. Bibliography.	82
1. Neutron Radiography	82
2. Sources	85
3. Geometry, Collimation and Analysis.	93
V RECOMMENDATIONS	95
VI REFERENCES.	97

ACCESSION NO.	
DTIC	Write Section <input checked="" type="checkbox"/>
DDC	Dev't Section <input type="checkbox"/>
UNANNOUNCED	<input type="checkbox"/>
JUSTIFICATION	
BY	
DISTRIBUTION/AVAILABILITY CODES	
UNCL.	AVAIL. and/or SPECIAL
A	

DDC
RECEIVED
 APR 24 1978
RECEIVED
 D

Synopsis

↙
A study is presented on the possibilities of using cold neutrons for non-destructive evaluation (NDE). There are shown to be two sectors where cold neutrons can be effectively employed: (1) cold neutron radiography (CNR); and (2) small-angle neutron scattering (SANS).

CNR is an established method of radiography with low energy, long wavelength neutrons, enabling greatly improved contrast and resolution over normal radiographic methods. This improvement will be especially important for hydrogenous materials, for example, contained within thick steel sections (e.g., one mm of plexiglas imbedded between two 7 cm section of steel plates). The main limitations to the use of CNR are portability and expense of the cold neutron source. Thermal neutrons from reactors, following moderation, remain the most intense and most practical flux. However, this requires that CNR be done at a reactor location. Some possibilities of efficient source mobility do exist, and these will be discussed.

SANS represents a very real departure from normal radiography methods of NDE, in that SANS is actually a scattering method for detecting heterogeneities (10-10,000 Å) imbedded within a matrix of different neutron scattering power. Though there are a number of subtleties that occur in the use of this method, SANS has been employed by workers in Italy over a remarkable range of applicability, from predicting failure in nickel-base superalloy turbine blades to a study of debonding of fibers in carbon-carbon fiber composites. Again, as with CNR, applied SANS suffers from the need of a high flux of cold neutrons. The possibilities and limitations of SANS for NDE, with special reference to Naval needs, are examined. ↙

I. INTRODUCTION

Cold neutrons from the point of view of non-destructive evaluation (NDE) can be used in two ways: i) radiography and ii) diffraction. Neutron radiography is similar in concept to x-ray radiography; it is a method of shadowing and has a long tradition, and a large number of references. Radiography depends on the absorption of neutrons by matter, there being lower absorption when there is a defect (e.g., crack) in the material under investigation. Cold neutron radiography (CNR) is not quite so simple, having the additional important feature of enhanced selective absorption, so that, for example, a small amount of hydrogenous material contained within thick, solid sections of steel, can be imaged. The imaging is in real space, so the analysis is rather straight forward. Of course, as always with radiography, resolution and intensity will limit the usefulness of the method. In particular, since generally cold neutron fluxes are low, detection presents special difficulties and much work has been dedicated to improving detectors (e.g., film with image-enhancing methods).

Scattering of cold neutrons by internal heterogeneities or internal products of plastic deformation (imperfections), represents a well-established method of examining alloy systems. In particular, small-angle x ray scattering (SAXS) has been employed with considerable success to characterize those second phases responsible for strengthening in precipitation hardenable alloys. SANS follows on the heels of SAXS, but offers new possibilities using standard approaches. Thus, SANS can be used to follow precipitate size in prototype studies in light alloy development. Or, as will be seen in this report, SANS can be used to follow the size and size distribution of coarsening γ' in

a superalloy blade used in a gas turbine engine.

But to analyze the SANS patterns normally requires a transformation from diffraction space (i.e., reciprocal space) to real space. This complex and frequently uncertain transformation can, however, be avoided by plotting the profile and comparing these to trial functions (that is, matching the obtained scattering profile against known and previously well-formulated profiles).

What we shall demonstrate here is the utility of SANS from an empirical point of view. For example, if we know how γ' develops in-use, say through metallographic means, than a comparison of the profiles obtained with SANS and the metallographic structure of the alloy gives us a good grasp of the condition of the alloy. If the conditions change, the γ' will change, and the strength properties will change. We want to empirically relate the varying SANS spectra to changing (degrading) properties.

The above approach has largely been taken by the FIAT Central Laboratory in Orbassano, Italy. P. Pizzi and H. Walther, using a SANS facility (dedicated by FIAT to applied work) at the GALILEO Reactor in Pisa, have studied a remarkable range of commercial alloy systems with SANS and have related the information obtained by SANS with that found by transmission electron microscopy (TEM). The comparison is excellent, especially for the complex multicomponent Inconel-type superalloys. (Appropriate references will be given in later sections).

It is of some importance to note that although there is clearly an overlap between the size ranges covered by SANS and that covered by TEM, these are basically complimentary techniques. SANS presents the further bonus of not having to destroy the specimen to determine what

is happening to the microstructure. Likewise, for SANS and CNR: SANS "sees" heterogeneities in the 10's to 1000's of \AA ranges, whereas CNR will detect heterogeneities and imperfections in the 10's to 1000's of micron range. What these two non-destructive techniques have in common is the need for a cold source; that is neutrons of low energy (e.g., $< 5 \text{ meV}$).

In the following shall be discussed sources of such neutrons, their spectral purity and how it is obtained. Mobility as well as expense are of central importance, but it is this writer's view that the question of the mobility of a truly portable high intensity cold neutron source is still uncertain and there may be very real future developments in this area (e.g., plasma focus).

SANS theory will then be briefly reviewed and those aspects of this theory that are useful for NDE will be emphasized. A number of important applications will be reviewed; with particular reference to gas turbine superalloys, the Ni-base multicomponent alloys which are strengthened by a fine and rather stable dispersion of the γ' inter-metallic particles based on $\text{Ni}_3(\text{Al}, \text{Ti})$.

Workers at the FIAT Central Research Laboratory in Orbassano, Italy (outside of Turin) are clearly the world leaders in applying SANS to actual technological alloys. Pizzi and Walther of FIAT have collaborated in this work and have achieved notable success. It can be concluded at this time that the results of their feasibility studies are highly satisfactory. Clearly, the initial results are exciting.

The Italians have developed a new philosophy of NDE in engineering alloys. The extent of their success can be seen by the continuing support given to their efforts by FIAT, who, it is my understanding, is using this NDE approach as a portion of their aspect of an international

licensing agreement with other manufacturers in gas turbine technology.

The Italians, however, are seriously limited in developing this new NDE approach due to the low flux of the GALILEO Reactor in Pisa. It commonly takes them hours to do a scattering experiment that might take 10 - 30 minutes to carry out at ILL-Grenoble in France or eventually, at Brookhaven National Laboratory in the U.S.A. (Brookhaven will by March, 1978, be the only high flux reactor facility in the U.S.A. with a cold source).

Thus, in a cooperative program among the Italians, Germans, French and British (who eventually dropped out) the reactor at ILL has been and will be continued to be used increasingly for applied work. The Jülich reactor (KFA) has also been brought into this Common Market-supported program. (The Germans, for example, are studying the evolution of pearlite in a eutectoid steel).

The British are now entering into various SANS programs. They have cooperative studies underway at ILL-Grenoble and have, together with workers at ILL, actually studied in situ creep of a "technological alloy". The British who are involved in this SANS study are located at AWRE, Aldermaston, where CNR is also a major activity. R. Miller and E.M. Gunnerson, who are mainly responsible for the SANS program at AWRE, have established a fine facility, and have, in fact, this November received their long-awaited L.E.T.I. area detector, which is the heart of any advanced SANS system. The AWRE team uses the HERALD Reactor in which is incorporated a D_2/H_2 cold source.

In the following will be discussed mainly SANS, theory and methods, followed by applications, with emphasis on the FIAT results. CNR will be discussed briefly, with the main contribution here being a recent

examination of the available literature, from the point of view of sources and application.

It is hoped that the future will see a more general application of cold neutrons for SANS and CNR in NDE for Naval programs both in the air and at sea.

II. NEUTRON SOURCES

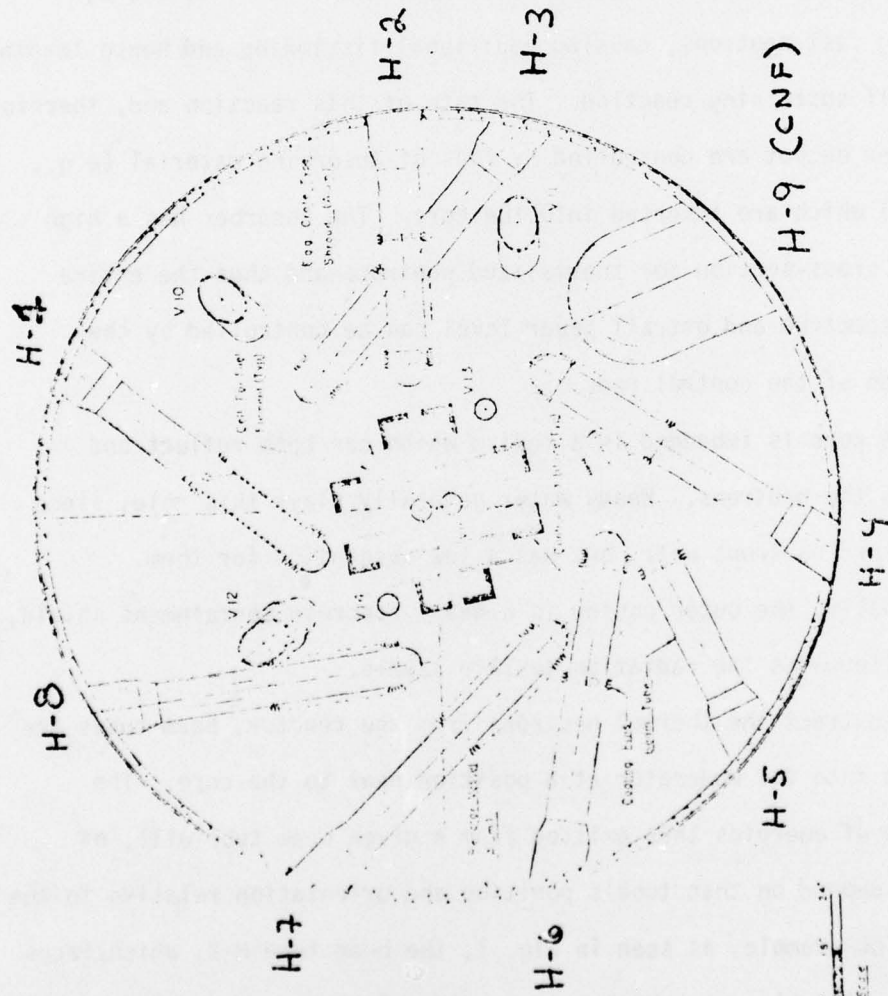
A. Steady State Reactors as Sources for Thermal Neutrons

A plan-view cross section of a modern research reactor (of the sort which are used to perform radiation damage or diffraction experiments) is depicted in Fig. (1). The core of the reactor is comprised of natural uranium (or of uranium enriched with U^{235} isotope) immersed, generally, in a heavy water moderator. U^{235} fissions, emitting fast neutrons, causing additional fissioning and hence leading to a self sustaining reaction. The rate of this reaction and, therefore, the power output are controlled by rods of absorbing material (e.g., cadmium) which are inserted into the core. The absorber has a high capture cross-section for thermalized neutrons and thus the entire energy spectrum and overall power level can be controlled by the insertion of the control rods.

The core is imbedded in a medium which can both reflect and moderate the neutrons. Heavy water generally plays this role, since it scatters neutrons well, but has a low absorption for them.

Finally, the outer casing is a heavy concrete containment shield, which attenuates the radiation to safe levels.

To extract the thermal neutrons from the reactor, beam tubes are inserted into the moderator at a position near to the core. The spectrum of energies thus emitted from a given beam tube will, of course, depend on that tube's position and orientation relative to the core. For example, as seen in Fig. 1, the beam tube H-2, which faces the core directly has a higher proportion of fast neutrons (for fast chopper experiments) than do the tangentially oriented tubes H-3



Neutron Exit Tubes	Neutron Exit Tubes
H-1	H-10
H-2	H-11
H-3	H-12
H-4	H-13
H-5	H-14
H-6	H-15
H-7	H-16
H-8	H-17
H-9	H-18
H-10	H-19
H-11	H-20
H-12	H-21
H-13	H-22
H-14	H-23
H-15	H-24
H-16	H-25
H-17	H-26
H-18	H-27
H-19	H-28
H-20	H-29
H-21	H-30
H-22	H-31
H-23	H-32
H-24	H-33
H-25	H-34
H-26	H-35
H-27	H-36
H-28	H-37
H-29	H-38
H-30	H-39
H-31	H-40
H-32	H-41
H-33	H-42
H-34	H-43
H-35	H-44
H-36	H-45
H-37	H-46
H-38	H-47
H-39	H-48
H-40	H-49
H-41	H-50
H-42	H-51
H-43	H-52
H-44	H-53
H-45	H-54
H-46	H-55
H-47	H-56
H-48	H-57
H-49	H-58
H-50	H-59
H-51	H-60
H-52	H-61
H-53	H-62
H-54	H-63
H-55	H-64
H-56	H-65
H-57	H-66
H-58	H-67
H-59	H-68
H-60	H-69
H-61	H-70
H-62	H-71
H-63	H-72
H-64	H-73
H-65	H-74
H-66	H-75
H-67	H-76
H-68	H-77
H-69	H-78
H-70	H-79
H-71	H-80
H-72	H-81
H-73	H-82
H-74	H-83
H-75	H-84
H-76	H-85
H-77	H-86
H-78	H-87
H-79	H-88
H-80	H-89
H-81	H-90
H-82	H-91
H-83	H-92
H-84	H-93
H-85	H-94
H-86	H-95
H-87	H-96
H-88	H-97
H-89	H-98
H-90	H-99
H-91	H-100

Fig. 1 Cross-section of Brookhaven National Laboratory HFBR showing neutron exit tubes and cold source, H-9 (CNF).

through H-8, which are for thermal neutrons. H-9, which is a cold source, acts as a source for particularly low energy neutrons and will be discussed later in more detail.

The emitted neutrons are, at least ideally, thermalized with energies corresponding to the temperature of the moderator. Actually, even with the greatest care of beam tube placement (preferably tangential to the core), the exiting thermal flux contains a fair proportion of fast neutrons and γ -radiation as well. This problem, as we shall see below, can be mitigated by monochromatization techniques and by transporting the thermal neutrons through guide tubes to a long distance from the reactor face.

Thermally, reactor neutrons can be considered to behave as monatomic gas molecules in a closed system, resulting in a Maxwellian velocity distribution, which is determined by the reactor ambient temperature (i.e., 50°-100°C). That is, they readily attain thermal equilibrium at the reactor ambient temperature, T , such that the average wavelength of the thermalized neutron will be

$$\lambda_n = h/\sqrt{3mkT} \quad (1)$$

where h is Planck's constant, m is the mass of the neutron, and k is Boltzmann's constant. For example, the root-mean-square wavelength of neutrons in equilibrium at 0°C is 1.55 Å, which is comparable with 1.54 Å of $\text{CuK}\alpha$ x-ray radiation, so commonly employed in crystallography measurements.

Neutrons will "leak" out through the exit beam tube at a flux such that the number emerging per second, $v_\lambda d$, with wavelengths between

λ and $\lambda + d\lambda$ is

$$v_{\lambda} = (2N_1/\lambda) [E(\lambda)/kT]^2 \exp[-E(\lambda)/kT] \quad (2)$$

where N_1 is the total flux of neutrons and $E(\lambda)$ is the energy of a neutron of wavelength λ .

The flux-wavelength distribution is depicted in Fig. 2 which gives the Maxwellian spectra for three different temperatures. This distribution is to be contrasted to the I -vs- λ curve for x-rays, where there are intense characteristic peaks related to the transitions which occur among the electron shells. For neutrons, in order to achieve monochromatization, it is required to employ a crystal monochromator or a mechanical velocity selector, frequently in combination with band pass filters of various types (1,2).

B. Other Sources

Both intensity and spectral distribution are important considerations in evaluating potential sources of neutrons. Broadly speaking, there are three source types: i) reactors; ii) nuclear reactions from accelerators; iii) radioactive decay.

Reactors of the steady state type, where fast neutrons originating from nuclear fission and which are moderated either by heavy water or graphite, represent the most effective neutron sources. Of special interest to us here are the medium-to-high flux reactors, which yield sufficient neutron fluxes so that diffraction and radiography experiments can be carried out in a reasonably short time (e.g., less than an hour). Reactors were discussed in Section IIA. For radiography with

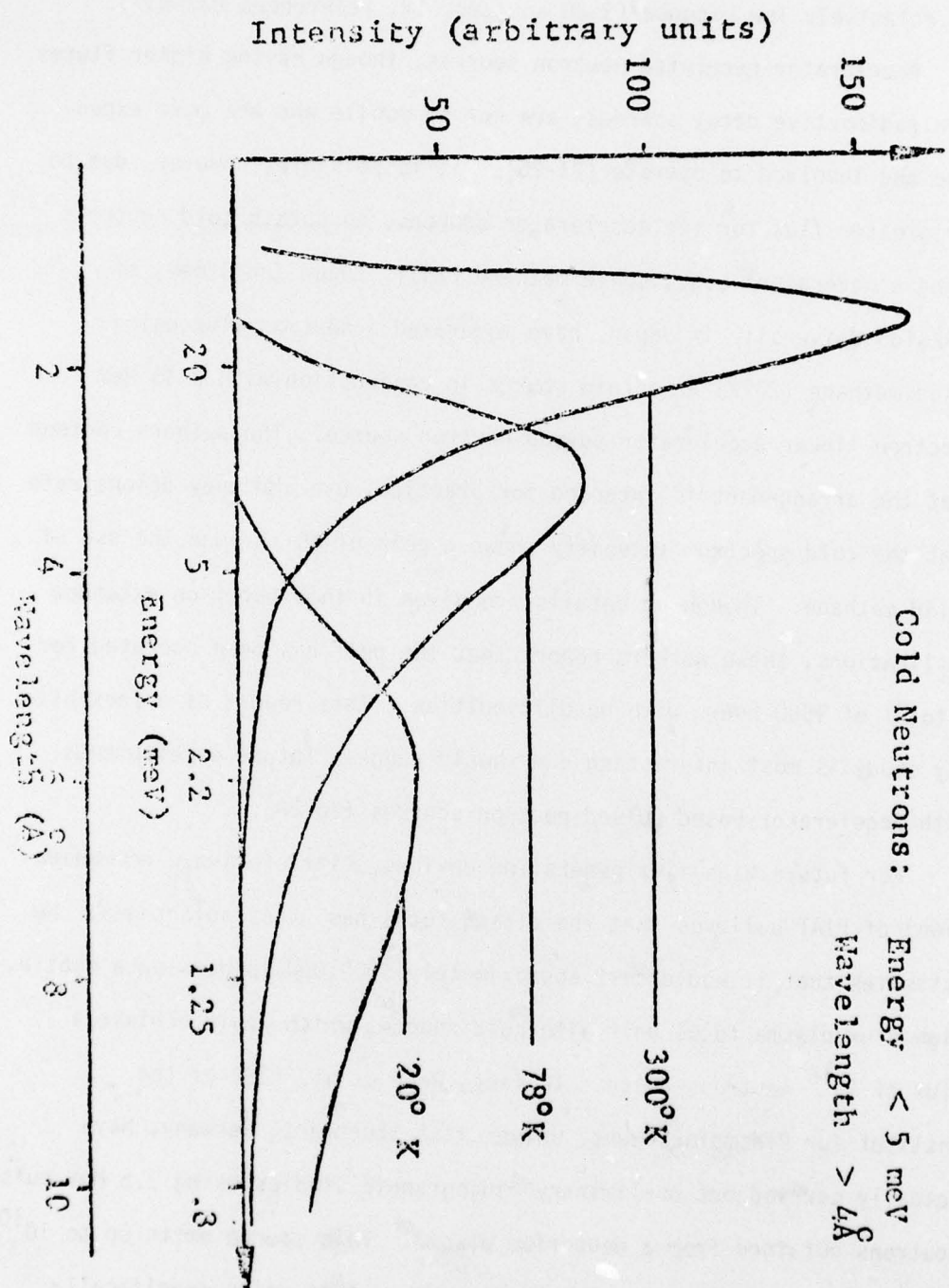


Fig. 2 Maxwellian spectra corresponding to different temperatures.

neutrons, the decay of Cf^{252} has been of great interest due to mobility and relatively low expense (3-20 and Sec. IV, references R32-R37).

Accelerator-generated neutron sources, though having higher fluxes than radioactive decay sources, are not so mobile and are more expensive and involved to operate (21-25). It is possible, however, due to the greater flux for the accelerator sources, to obtain cold neutrons using a moderator; e.g., solid methane (25). Inoue and Otome, of Hokkaido University in Japan, have moderated a neutron flux using solid methane (20°K) as a cold source in conjunction with a 45 MeV electron linear accelerator pulsed neutron source. The authors contend that the arrangement is intended for practical use and they demonstrate that the cold spectrum intensity shows a gain of 40 through the use of solid methane. Though no details are given in this paper on extended applications, these workers report that the unit has been operated for a total of 1500 hours with no difficulties. This report of a feasibility study is most interesting and should suggest future developments with accelerator-based pulsed neutron sources (26-28).

For future high-flux generating devices, Pizzi (private communication) of FIAT believes that the plasma focus has great advantages. He estimates that it would cost approximately \$500,000 to develop a mobile, high-flux plasma focus unit with cold source, which would achieve a flux of 10^{15} neutrons/pulse. In fact, Rapp et al. (29) of the Institut für Plasmaforschung, Universität Stuttgart, Germany, have actually carried out preliminary radiographic studies using 2.5 MeV pulsed neutrons obtained from a deuterium plasma. This source emits up to 10^{10} neutrons within 100 nsec. The authors argue that units specifically designed for radiography could be mobile and relatively inexpensive

(29A-D; also see Sec. IV, ref. R30). The main issue treated in the Rapp et al. paper (29) is the sensitivity of the detector for low neutron fluxes. It remains to be seen if the plasma focus concept can be developed as a high-flux generator of neutrons.

Another innovation in high flux neutron generation is based on the tritium ion beam. A flux of greater than 10^{14} neutrons/cm² per second of 14 MeV neutrons will be generated from the collisions of two intersecting beams; one of 270 KeV tritium ions and the other, a supersonic jet of deuterium molecules. Focusing of the resulting neutrons may be difficult to achieve, and thus the efficiency of this sort of source for either radiography or SANS is uncertain. A paper by Emigh describes the technique (29E).

A pulsed neutron source is operational at Dubna near Moscow. This is the IBR-30 and it is currently operating at a average power level of 25KW, but will be soon upgraded to 250 KW average power. It is my understanding that diffraction experiments are being carried out on this source. One point of interest: the Russians lack the computer hardware needed to use a area detector for SANS. Until this situation is changed, it is not likely that they will be serious competitors in this field.

In Table I is shown the various types of neutron sources which have been discussed. References to the major literature discussions are given in Sections IV and V.

TABLE I

Neutron Sources

Source	Reaction	Flux	References
Cf^{252}	Fission	$2 \times 10^9 \text{ sec}^{-1}$	3 - 20A, B, C (R32 - R37)
<u>Accelerator</u>			
$\begin{pmatrix} 300 \text{ KeV} \\ @ 8 \text{ ma} \end{pmatrix}$	T(d,n)He^4	10^{12} sec^{-1}	21 - 28 (R18, R18A R21, R22, R23, R27)
$\begin{pmatrix} 4-8 \text{ MeV} \\ @ 0.4 \text{ ma} \end{pmatrix}$	$\begin{pmatrix} \text{Be}^9(\text{d,n}) \text{B}^{10} \\ \text{Li}^7(\text{p,n}) \text{Be}^7 \end{pmatrix}$	$\begin{pmatrix} 10^{12} - \\ 10^{13} \text{ sec}^{-1} \end{pmatrix}$	
Plasma Focus	D(T,n)He^4	$10^{15}/\text{pulse}$	29, 29A-D (R30)
5 - 40 MW Steady State Reactor	Fission	$10^{13} -$ $10^{16} \text{ sec}^{-1} \text{ cm}^{-2}$	1 - 2 (R19, R24, R25, R26, R28)

C. Reactors with SANS and Cold Neutrons

Relative to the high and medium flux reactors operating today with a cold source, specifications are given below for:

D 11A, ILL-Grenoble; HFBR, Brookhaven National Laboratory;
FRJ-2, KFA, Jülich; GALILEO, FIAT, Pisa; HERALD, AWRE, Aldermaston;
respectively in Tables II - VI.

Table II (France)

D11A SANS Facility at the Institut Laue-Langevin, Grenoble, France

(Note: ILL is operated jointly by France, Germany and the U.K.)

Reactor Power: 57 MW

Instrument details

Beam-tube	: H 15 (cold neutron guide)
Monochromator	: Helical slot selector (or double crystal)
Maximum flux at specimen	: $10^5 - 10^8 \text{ sec}^{-1} \text{ cm}^{-2}$ (depending on λ and angular resolution)
Maximum beam-size at specimen	: $\phi = 10 \text{ cm}$
Incident wavelength	: $3 < \lambda (\text{\AA}) < 20 \text{\AA}$
Energy range (for inelastic measurements)	: $10^{-6} \text{ eV} < E < 10^{-1} \text{ eV}$
Q-range ($Q = \frac{4\pi \sin \theta}{\lambda}$)	: $10^{-4} < Q (\text{\AA}^{-1}) < 1$
Wavelength resolution (mean squared deviation)	: $\frac{\Delta\lambda}{\lambda} = \pm 3 \%$ over the whole Q-range
Angular resolution (mean squared deviation)	: $\frac{\Delta\theta}{\theta} = \pm 3 \%$ at a mean Q-value (for each detector position)
Q-resolution (mean squared deviation)	: $\frac{\Delta Q}{Q} = 4 \%$
Detectors:	
- Two dimensional set of	: 64 x 64 channels
- Ionization chamber type	: (BF ₃)
- Cross-section of channel	: $10 \times 10 \text{ mm}^2$
- Max. counting rate	: $5 \times 10^4 \text{ c/s}$
- Installation of detector possible at 40; 20; 10; 5 and 2 m distance from the sample, corresponding to collimation length.	
Ancillary equipment for sample:	2 cryostats for variable temperature $4, 2^\circ\text{K} < T < 300^\circ\text{K}$

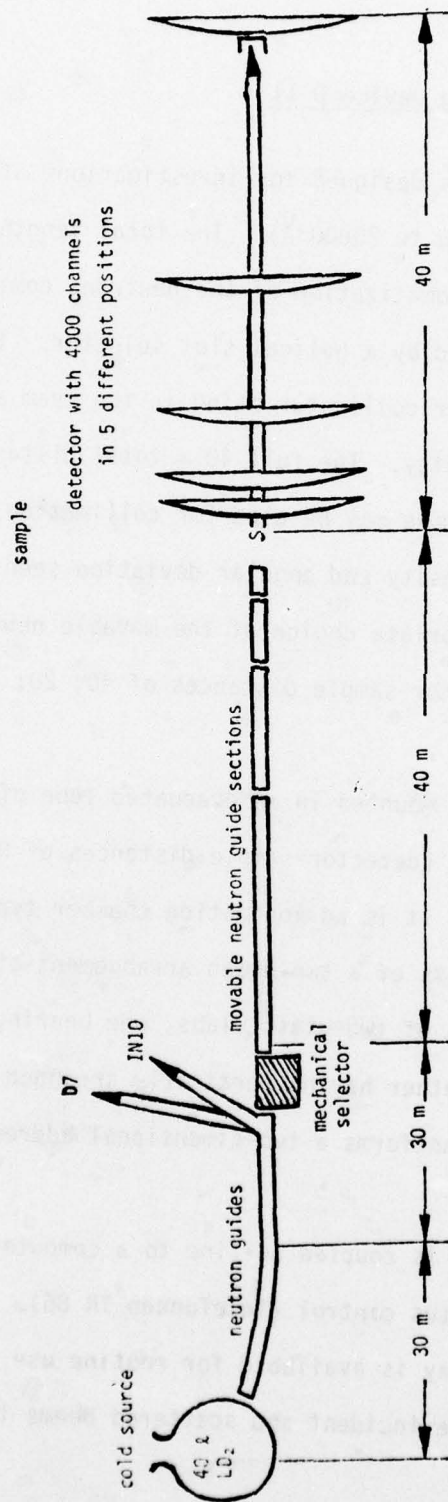
Table II - Continued

Small Angle Scattering Device D 11

The instrument is designed for investigations of large structures (inhomogeneities from 5 to 20000 Å). The total length of the instrument is 80 m. The monochromatization of the neutrons coming from the guide-tube is achieved by a helical slot selector. These slots have the effect of a Soller collimator being in the beam axis for neutrons of a particular velocity. The full 40 m total distance between monochromator and sample may be used for collimation for high resolution work. The intensity and angular deviation seen by the sample can be selected by appropriate choice of the movable neutron guides. Effective monochromator-sample distances of 40; 20; 10; 5 and 2 m are available.

The detector is mounted in an evacuated tube of 40 m length with 5 possible positions (detector-sample distances of 0.66 and 1.30 m are also possible). It is an ionization chamber type (BF_3 at atmospheric pressure) and consists of a two-dimen arrangement of 64 x 64 channels. The counter consists of two glass slabs, one bearing horizontal strips of electrodes, the other having vertically arranged electrodes. A coincidence unit transforms a two-dimensional address into Cartesian coordinates.

The instrument is coupled on-line to a computer for data acquisition and for apparatus control (Telefunken TR 86). A program for data reduction and display is available for routine use, while a program for deconvolution of the incident and scattered beams is in preparation. (Ref. 2, 30-35).



NEUTRON SMALL ANGLE CAMERA D11

Table III (U.S.A.)

Brookhaven National Laboratory, Upton, L.I., N.Y.

High Flux Beam Reactor with Proposed SANS Facility.

The Cold Neutron Source will be operational in 1978.

Reactor power	40 MW
Total fast neutron flux, fuel region	$1.6 \times 10^{15} \text{ n/cm}^2\text{-sec}$
Maximum thermal flux, reflector	$0.7 \times 10^{15} \text{ n/cm}^2\text{-sec}$
Active core volume	97 liters
Active height of core	52.7 cm.
Diameter of core (equivalent cylinder)	47.8 cm.
Number of fuel elements in core	28
Dimensions of fuel element	
Cross section (19 fuel plates)	8.113 x 7.163 cm.
Length of 2 outer fuel plates	58.4 cm.
Length of 17 inner fuel plates	52.7 cm.
Total length of fuel element	154.4 cm.
Uranium-235 content of fuel element	315 g
Total uranium-235 loading	8.8 kg
Reactor coolant	heavy water (D ₂ O)
Total coolant flow rate	1150 l./sec.

Proposed SANS Facility

Beam Size	$1.27 \times 4.4 \text{ cm}^2$
Monochromator	Velocity Selector or Multilayer
Wavelength	$\lambda = 8 \text{ \AA}$
$\Delta\lambda/\lambda$	10%
Best Resolution	$\sim 2 \times 10^{-4} \text{ \AA}^{-1}$

L = 8 M

Table III (Continued)

Smallest Angle	
L = 8 M	.06° (1 mrad)
Largest Angle	10°
Detector	18 x 18 cm ² position sensitive
Resolution	3 mm
Count Rate	10 ⁴ /sec.

Table IV (Germany)

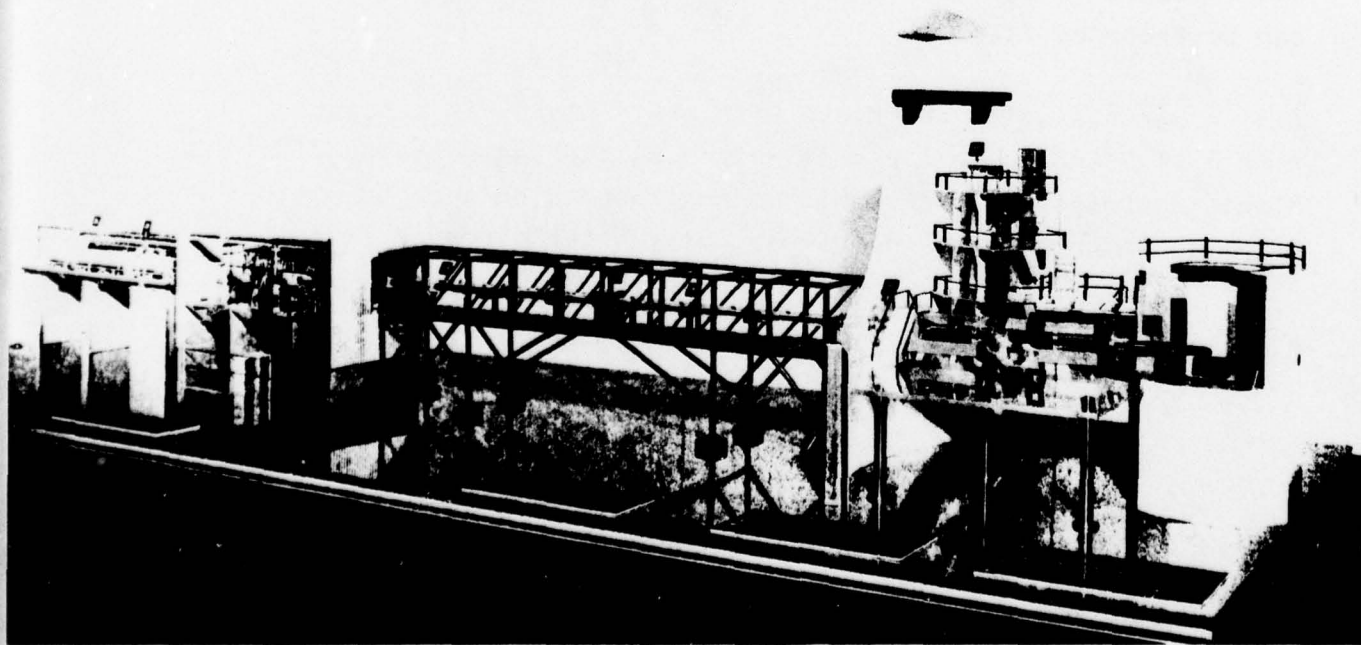
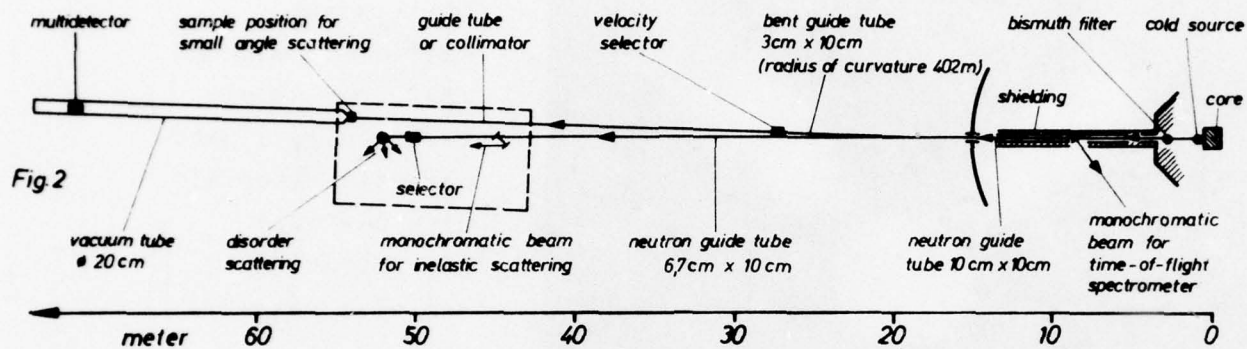
FRJ-2 (DIDO) Reactor at
 Institut für Festkörper-und-Neutronenphysik, KFA
 Jülich, W. Germany

Total length: 40 M

Cold moderating source of liquid hydrogen connected to SANS instrument
 by total-reflecting neutron guide.

Monochromatization performed by mechanical velocity selector, consisting
 of a rotating drum with helically curved slits, yielding wavelength
 to $\pm 10\%$. The wavelength range is 4 to 20 Å.

Detector: two-dimensional detection obtained by a number of position
 sensitive propositional counters (5 cm diam. x 60 cm long) with an
 axial resolution of 1 cm and a sensitivity of 70% at 10 Å. A schematic
 diagram of the SANS unit of FRJ-2 is given below. (Ref. 2, 30).



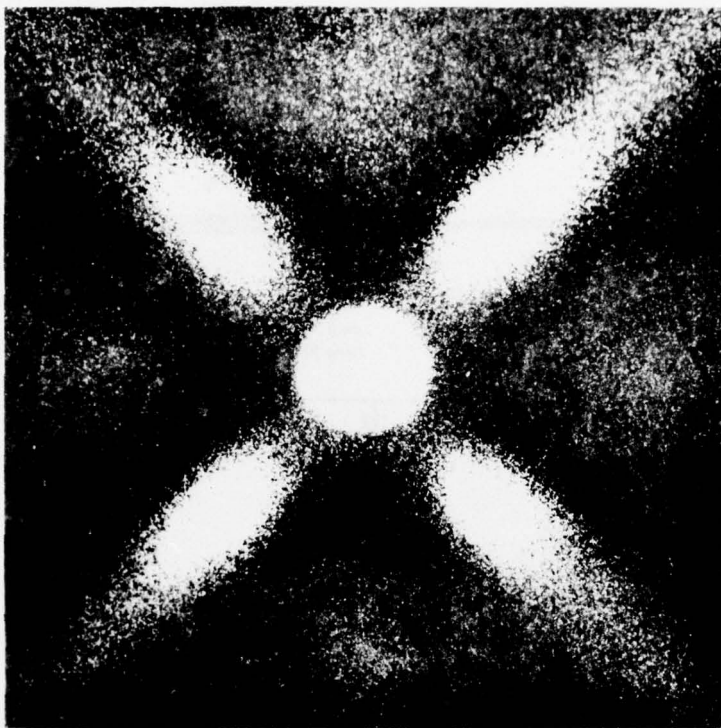


Fig. 4
 photograph of
 small angle
 scattered neutrons
 /19/. The sample
 is Ticonal, a hard
 magnetic material
 with periodic
 precipitations
 (see also ref./2/).

total length of 60 cm. Counting rates as high as 20,000 per sec.
 can be recorded /17/.

(ii) A scintillation technique with photo-plates in contact
 with a $\text{Li}^6\text{F-ZnS}$ layer for small-sized scattering patterns /18/.
 Single neutrons are observable as small spots on a photo-plate
 (fig. 4) which is scanned automatically after exposure /20/.

Jülich, 4th August 1969
 Institut für Festkörper- und
 Neutronenphysik - Neutronenphysik
 Kernforschungsanlage Jülich GmbH.
 517 Jülich, Postfach 365
 W.-Germany

GALILEO (CAMEN-Pisa) Reactor (FIAT)

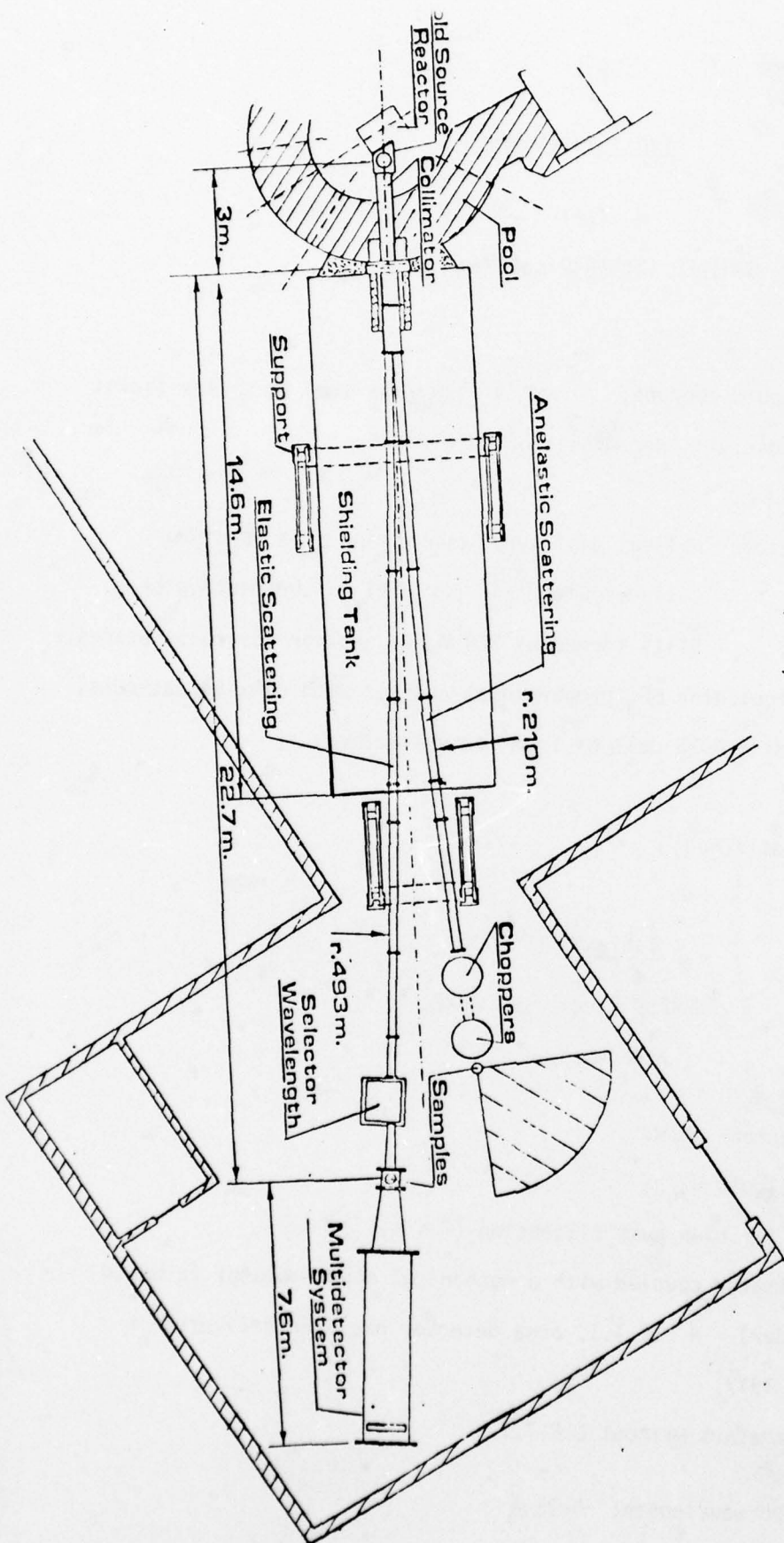


Table V (Italy)

FIAT

GALILEO (CAMEN-Pisa) Reactor

Power: 5 MW

Cold Source: Liquid propane; of a flow rate such that significant radiolytic decomposition is avoided.

Total length: 33 m.

Wavelength selector: Helical slit type, consisting of a rotating cylinder with axis parallel to the neutron beam.

Slits formed by 258 Mg-Cd neutron absorbing blades.

Detector: Multicellular BF_3 proportional counter with 64 x 64 cathodes, yielding 4096 cells of 1 cm² cross-section.

(Ref. 36)

(See Schematic attached)

Table VI (U.K.)

HERALD Reactor at AWRE

Aldermaston, U.K.

Medium Flux Reactor: 5 MW

Cold Source: liquid H_2/D_2

Cold Be filter for high pass filtration ($\approx 4 \text{ \AA}$).

Fine Slit collimator coupled with a mechanical monochromator (a Mg-Cd alloy cylinder). A L.E.T.I. area detector has been delivered in November of 1977.

Instrument parameters without L.E.T.I.

Incident neutron wavelength: 6-25 \AA

Table VI (Continued)

Wavelength resolution: 8%

Flux at sample at 6 \AA : $2 \times 10^2 \text{ n mm}^{-2} \text{ sec}^{-1}$ (5 MW)

Beam size at sample: 30 mm wide x 20 mm high

Detectors: 10 BF_3 type 40EB 140/50G

6 BF_3 type 50EB 140/50G

1 BF_3 type EB 70/50G

(Ref. 37)

III. SMALL-ANGLE NEUTRON SCATTERING

The theory of small angle scattering of both x-rays and of neutrons are identical, except for some details (e.g., scattering strengths, angular variations). In the following will be given the elementary theory of neutron-matter interactions. This will be followed by an introduction to aspects of small angle scattering theory.

A. Interactions of Neutrons with Matter

1. Absorption

Due to their electrical neutrality, neutrons are generally little absorbed by most solids, and, therefore, have large transmission coefficients. However, there are important exceptions to this: boron, cadmium and gadolinium have high capture cross-sections for neutrons having wavelengths in the range of 1 \AA . The process involves a resonance excitation, each of the above atoms having a different critical energy for this process. Neutrons having energies higher than this critical energy will be absorbed, whereas neutrons having energies

below this excitation value cannot be absorbed and thus are transmitted (but are scattered due to the virtual interaction that operates between the nucleus and the neutron). This effect gives rise to a neutron energy edge, and hence, just as for the case of x-rays, an absorption filter monochromator may be devised (1).

2. Scattering

A beam of neutrons, emanating from a reactor port, can be employed for diffraction experiments if the energy of the neutron is sufficiently low. For example, a neutron with a velocity of 2 km/sec has an energy of 0.02 eV, and a wavelength of 2 \AA .

Note that the energy associated with x-rays is of the order of 10^4 eV, while for phonons within crystals the energy is of the order of 0.01 eV, which is much closer to that of neutrons. It is thus possible to employ neutron scattering methods to examine the thermal or phonon properties of the atomic vibrations within a crystal lattice. The neutrons can exchange energy with the vibrating lattice, and this diminished neutron energy can be measured and related to the phonon spectra within the crystal. This inelastic scattering property of the neutron is different from the elastic scattering which treats the atoms as being rigidly placed in specific locations within the lattice. It is elastic scattering which interests us here, since this permits us to determine these positions.

For our present needs, we shall consider two mechanisms of neutron scattering: (1) magnetic and (2) nuclear (hard sphere, elastic) scattering. We shall be concerned primarily with the latter, but it is important to note that neutron scattering studies of magnetic materials have

contributed an enormous amount of information on the crystal structure and atomic arrangements within these important classes of materials (1, 30, 38).

In elastic scattering the nucleus of an atom scatters the neutron as if the nucleus were a hard sphere of radius 10^{-12} cm. In x-rays, the atomic scattering factor, $f(2\theta)$ is a function of scattering angle, and the value approaches the atomic number, Z , at zero scattering angle. This is because the atom has a finite dimension, from the point of view of the wavelength of the x-ray radiation. This is not the case for elastic scattering of neutrons by the nucleus, where the wavelength and scatterer diameter are not of comparable dimension. Thus, the nuclear scattering power, known as scattering length, b , is not angularly dependent. (There will be an angular dependence, however, when magnetic scattering is considered.) This effect is illustrated in Fig. 3 (after Shull, Ref. 38).

The amplitude scattered by a crystal with only one atom per unit cell will thus be

$$A(\bar{Q}) = b \sum_{\ell} \exp(i\bar{Q} \cdot \bar{r}_{\ell}) \quad (3)$$

where $\bar{Q} = \bar{k}_1 - \bar{k}_0$ is the difference between the incident and scattered waves. Assuming that all the atoms are fixed in position and that the scattering is elastic, $|\bar{k}_1| = |\bar{k}_0|$. It can be shown that under these conditions, Eq. (3) reduces to

$$A(\bar{Q}) = \frac{(2\pi)^3}{V} b \sum_{\mathbf{h}} \delta(\bar{Q} - \bar{Q}_{\mathbf{h}}) \quad (4)$$

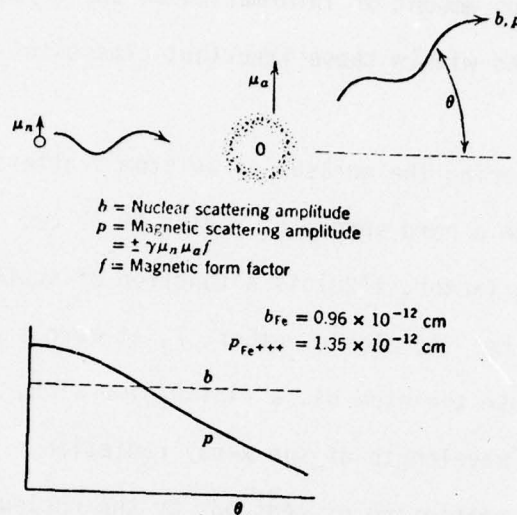


Fig. 3 Neutron scattering by a magnetic atom illustrating both nuclear and magnetic scattering. After Shull, Ref. 38.

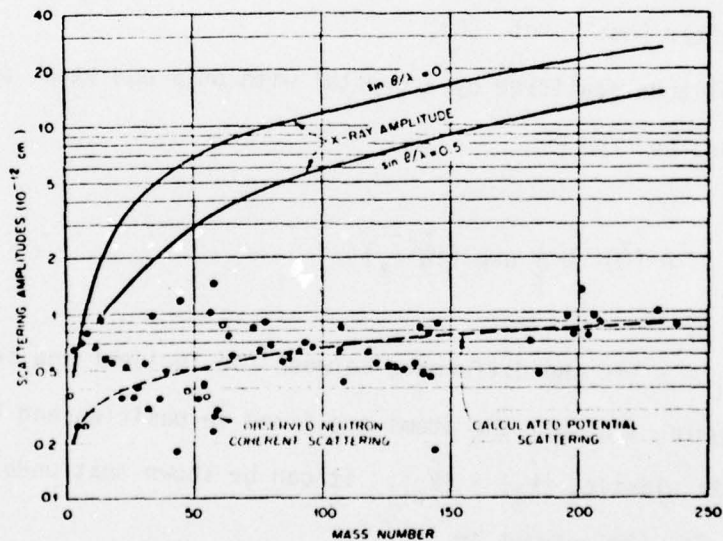


Fig. 4 Variation of scattering amplitude with atomic mass number for x-rays and neutrons. After Shull, Ref. 38.

where $\delta(\bar{Q} - \bar{Q}_n)$ has the properties of a three-dimensional Dirac δ -function, requiring that the neutron amplitude that is scattered be zero unless the scattering vector is also a vector to a point in reciprocal space. Therefore, $\delta(Q) = 0$, except when \bar{Q} coincides with \bar{Q}_n .

When there are several atoms per unit cell, b must be replaced by b_j , which is the scattering length of a given atom j . Thus, the structure factor is

$$A(\bar{Q}_n) = \sum_{j=1}^n b_j \exp(i\bar{Q}_n \cdot \bar{r}_j) \quad (5)$$

The intensity scattered by this array of atoms gives Bragg reflection intensities, $|A(\bar{Q}_n)|^2$, and it these intensities which are measured in neutron diffraction experiments.

The standard elastic scattering equation for neutrons, including the major terms, is shown in standard texts (e.g., Bacon, 1975; Ref. 1) to be more complex than that given by Eq. (5), where only coherent scattering terms are considered. Isotopes of the same element will not, for example, necessarily have the same scattering length. For the case of iron, Fe^{54} , $b = 0.42 \times 10^{-12}$ cm, whereas for Fe^{56} , $b = 1.01 \times 10^{-12}$ cm. Thus, for a crystal of iron, b cannot be assumed to be identical for both isotopes and we have for the scattered amplitude:

$$A(\bar{Q}) = \bar{b} \sum_{\ell} \exp(i\bar{Q} \cdot \bar{r}_{\ell}) + \sum_{\ell} (\bar{b}_{\ell} - \bar{b}) \exp(i\bar{Q} \cdot \bar{r}_{\ell}) \quad (6)$$

where \bar{b} is an average of the scattering lengths. The first term on the

right is that for coherent elastic diffraction of neutrons and gives peaks of diffracted energy at the nodes of reciprocal space. The mean square value of the second term is $N[\overline{b^2} - (\overline{b})^2]$ and represents a uniform background scattering. This general incoherent scattering is similar to that arising in alloy solid solutions, i.e., Laue monotonic. We will return to this subject later when clustering in alloys is discussed.

An important difference between neutron scattering and x-ray scattering is the variation of scattering length or scattering amplitude with mass number. It is well known that x-ray scattering factors depend in a continuous manner on atomic number. This is due, of course, to the fact that x-rays are scattered by electrons. Neutrons, however, are scattered in a non-continuous manner, and the scattered amplitude does not depend on atomic number in a predictable, simple manner. This is seen in Fig. 4 (after Ref. 38), where the scattering amplitudes for x-rays and neutrons are plotted against mass number. This effect is particularly important for SANS since it is necessary for the scattering particle and matrix to have scattering strengths of sufficient difference to be apparent at small angles. Thus, Al and Mg are adjacent on the periodic chart and give low scattered intensity for SAXS, but they give high intensity for SANS, since their coherent scattering lengths differ sufficiently.

3. SANS Theory

The coherent scattering of neutrons is a consequence of the interaction of the neutrons with nuclei throughout the material. The secondary rays scatter in all directions, but because phase

relations are preserved on scattering, interference with rays from adjacent scattering centers will occur so that the particular distribution of scattered intensity observed is a function of spatial arrangement of the nuclei, i.e., the atoms comprising the material.

Small-angle neutron scattering refers to the coherent scattering of neutrons at angles below a few degrees (5°) 2θ , i.e., the angle between the rays of incident and scattered beams.

The scattering diagram is given in Fig. 5a. \vec{k}_0 is the incident neutron wave and \vec{k} is the wave scattered from a point in the specimen by a scattering angle $\epsilon = 2\theta$, to a position on the detector plane. The detector, for SANS studies, will, it is assumed, always be an area detector. A one-dimensional scan of the detector is shown schematically in Fig. 5b.

Broadly speaking, three types of scattering phenomena can be observed at small angles: Fig. 5b. First, discontinuous, where scattering is favored at specific angles (small angle diffraction) and is usually a consequence of definite, large lattice spacings in the sample. Secondly, beam broadening arising from the refraction of the direct beam on passing through alternating media for which the refractive index of the neutron gives rise to actual refraction effects. The effect, though small, is measurable at small angles. As will be seen later the broadening arises from multiple refractions. The number of refractions, n , is given by $[(\Delta\epsilon)^2 - (\Delta\epsilon_0)^2]R$, where R is a constant determined by slit geometry and the shape of the scattering particles, and $\Delta\epsilon$ and $\Delta\epsilon_0$ are the half-width, respectively, of the broadened beam and the direct beam. Broadening results from the neutron alternatively passing thru regions of different indices

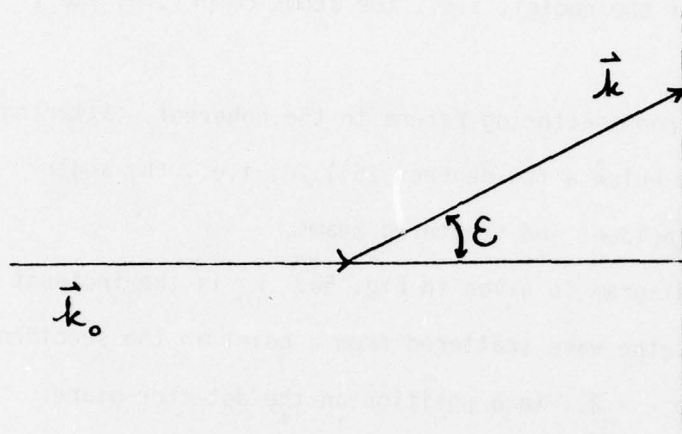


Fig. 5a Scattering Diagram. \vec{k}_0 is the incident neutron wave vector, \vec{k} is the scattered wave vector and $\epsilon = 2\theta$ is the scattering angle.

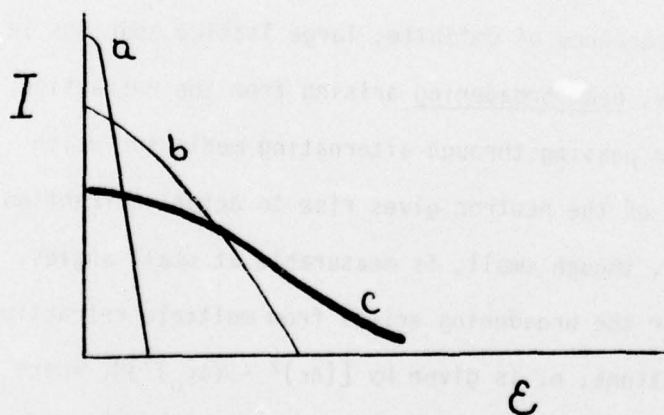


Fig. 5b Intensity profiles versus scattering angle. a) direct beam; b) refraction-broadened beam; c) diffracted intensity.

of refraction; e.g., magnetic domains, eutectoid products of decomposition. Beam broadening, which is not a true scattering process, has been shown by the Italian workers to be of some interest in applied work (Sec. IIIB2).

The third type of small angle scattering is continuous, where the scattered neutron intensity varies monotonically with angle. It arises from interactions with heterogeneous regions or particles more or less randomly distributed throughout the material. The term "particle" is used to denote any heterogeneity or region in which the neutron density is different from that in the surrounding material (e.g., voids). These particles may range in size from greater than atomic dimensions to thousands of angstroms. The continuous scattering is nearly independent of the internal structure of the particle, but is dependent to a large degree on particle size, shape and distribution.

The primary purpose of a small angle scattering experiment is to determine the angular distribution of the scattered intensity. Appropriate methods of analysis of these data provide information about parameters such as size, shape and distribution of the inhomogeneities. Determination of absolute values of intensities has assumed increasing importance, for it provides quantitative information on nuclear density. When used in conjunction with additional information, it is possible to precisely characterize the heterogeneities.

a. Radius of Gyration

The intensity of the small angle scattering is related

to the differences in coherent scattering length density between the particle and the matrix as well as to the number of scattering centers. In the case of groups of widely separated particles (dilute concentrations) which are randomly oriented, the scattered intensity is given by (39)

$$I(Q) = I_n(Q) N F^2(Q) \quad (7)$$

where N is the average number of scattering particles, $I_n(Q)$ is the intensity scattered by a single nucleus and $F^2(Q)$ is the average of the square of the structure factor of the particle and is also the Fourier transform of the shape of the particle. The quantity Q is given by

$$Q = \frac{4\pi \sin \theta}{\lambda} \quad (7A)$$

where λ is the wavelength of the incident neutrons and 2θ is the scattering angle.

The scattering intensity at very small angles can be closely approximated by

$$I(Q) = I_n(Q) N n^2 \exp[-Q^2 R_g^2/3] \quad (8)$$

where n is the number of nuclei per particle and R_g is the radius of gyration of the particles. Although strictly valid at zero scattering angle (for $|\bar{Q}|R_g < 1.5$), Eq. (8) is a sufficiently good approximation to represent the intensity curves over a finite region, especially

for spherical particles (39). Therefore, the radius of gyration can be determined from the slope in the straight-line region near zero angle of a plot of $\log I(Q)$ -vs- θ^2 . From Eq. (8), when θ is measured in radians, we obtain

$$R_g = \frac{\lambda}{4\pi} \left| \frac{3(-\text{slope})}{\log \theta} \right|^{1/2} \quad (9)$$

which can be used to calculate the radius of gyration. The radius of gyration is related to actual radius, R , for a set of spherical particles by

$$R = \sqrt{\frac{5}{3}} R_g \quad (10)$$

At sufficiently large angles (i.e., $R_g Q > 2.5$), the Guinier approximation is no longer valid.

The above procedure holds for a system of widely separated and randomly oriented particles. If the concentration of scattering particles is high or if their interaction is strong, the curve of $F^2(Q)$, will be deformed, and the apparent radius of gyration as-obtained from the Guinier plot will be smaller than the true value. Interparticle interference effects will also occur. These effects were first calculated by Zernike and Prins for the case of spherical particles and was extended to particles of general shape by Mencke and Fournet (See Ref. 40). Fournet has attempted to transform the Zernicke-Prins type equations, which concern only the geometry of the ensemble of particles, into "thermodynamic equations" by the introduction of certain intrinsic characteristics of particles. His equation

reduces, in dilute systems, to a form giving scattering from a single particle and shows that as the concentration increases, the effect of interparticle interference is usually to decrease the scattered intensity at the smallest angles and to have little or no effect on the outer part of the curve. It can be shown that the apparent radius of gyration is a linear function of the concentration at low concentrations (40). Hence, the usual method adopted to overcome the interparticle interference effects is to investigate a concentration series and to extrapolate the apparent radius of gyration to zero concentration.

Another assumption made in the above analysis is that all the scattering particles are identical. In the case of a collection of particles which are known to be polydisperse, it can be shown that the scattering curve still approximates to a Gaussian for sufficiently small values of Q . But now the radius of gyration will be an average in which the large radii of gyration are very heavily weighted. Attempts have been made to determine the statistical distribution of the particles from the shape of the curve using the Guinier approximation and assuming that all particles are geometrically similar and the distribution of sizes is represented by a Maxwellian (41, 42).

b. Determination of shape, volume and surface area

i) shape: The shape of the particles can be estimated by plotting the scattering curve, corrected for interparticle interference effects, as $\log I(Q)$ -vs- $\log Q$ and comparing the shape of the curve with the shape of the theoretical curves for uniform ellipsoids, cylinders, etc. See Table VII. It is, however, difficult

to distinguish details of shape and it is frequently assumed in practice that the particles are uniform ellipsoids of revolution and one attempts only to determine the best value for the axial ratio.

ii) volume: According to the theories of Debye and Bueche (43) as well as of Porod (44-47), for the case of a two phase system, the "invariant"

$$Q_i = \int_0^{\infty} I(Q) Q^2 dQ \quad (11)$$

depends only on the total volume of the dispersed phase, and is independent of the degree of dispersion; that is, the volume of the particle.

The zero value of intensity, $I(0)$, increases, for a fixed concentration, with the volume of the particles, as seen from,

$$I(0) = I_n(0)NV^2\rho^2 \quad (12)$$

V is the volume of the particle and ρ , its nuclear density. For a fixed concentration, NV and ρ are constant, and $I(0)$ increases with V . Hence, the quotient $I(0)/Q_i$ is a measure of the volume V of the particle. It can be shown that

$$\frac{I(0)}{Q_i} = \frac{V}{2\pi^2} \quad (13)$$

Thus, no absolute intensity measurements need be made to evaluate the volume of the particle.

iii) surface area: A detailed analysis of the treatment of the scattering functions for particle surface study is given in Ref.(39). Here will be outlined Porod's approach to surface-to-volume values for heterophase systems. Porod (44-46) has shown that for the special case of a two-phase system, each phase being of constant nuclear density and arbitrarily distributed,

$$\lim_{Q \rightarrow \infty} I(Q) = 2\pi I_n(Q)(\Delta\rho)^2 S Q^{-4} \quad (14)$$

where $\Delta\rho$ is the difference in nuclear density between phases 1 and 2 and S is the total area of the interface separating the phases. The absolute value of intensity at large Q , i.e., the higher angle region of the diffraction curve, depends then on only $\Delta\rho$ and S . The equation predicts that the outer portion of the scattering curve decreases asymptotically with Q^{-4} (Table VII). This fact is useful in confirming the existence of a sharp interface between the heterogeneities and the matrix and for establishing the range of Q over which the surface area measurements can be validly carried out. This method involves the absolute measurement of $\lim_{Q \rightarrow \infty} I(Q)$ and since $\lim_{Q \rightarrow \infty} I(Q) < I_0$, the intensity for the incident beam, this cannot be done satisfactorily.

To avoid the difficult measurement of I_0 , Porod introduced a normalization procedure (44). He showed that S/V , the surface-to-volume ratio, known as the specific surface, S_{sp} , can be expressed as

$$S_{sp} = \pi C_1(1-C_1) \left[\lim_{Q \rightarrow \infty} I(Q) Q^4 \right] \left[\int_0^\infty Q^2 I(Q) dQ \right]^{-1} \quad (15)$$

where C_1 is the fraction of the volume occupied by the phase 1. If

TABLE VII

Commonly used scattering cross sections (i.e., scattered intensity) in technological SANS studies (After Pizzi).

SCATTERER	SCATTERING CROSS-SECTION	$\frac{d\sum_s}{d\Omega} = I(Q)$	ASYMPTOTIC FORM
THIN DISK (2R=diam.)	$N V^2 (\Delta n)^2$	$\left[\frac{J_{3/2}(QR)}{(QR)^{3/2}} \right]^2$	$\frac{1}{Q^{-4}}$
THIN DISK (2R=diam.)	$\frac{N^2 V^2}{K^2 R^2} (\Delta n)^2$	$\left[1 - \frac{1}{QR} J_1(2QR) \right]$	$\frac{1}{Q^{-2}}$
THIN CYLINDER (2H=length)	$N V^2 (\Delta n)^2$	$\left[\frac{\text{sh}(2QH)}{QH} - \frac{\text{sen}^2(QH)}{Q^2 H^2} \right]$	$\frac{1}{Q^{-1}}$
SPHERICAL SHELLS	$N^2 V^2 (\Delta n)^2$	$\left(\frac{\sin QR}{QR} \right)^2$	$\frac{1}{Q^{-2}}$
GUINIER APPROXIMATION	$N V^2 (\Delta n)^2 \exp$	$\left[-\frac{Q^2 R^2}{3} \right]$	
RANDOM FLUCTUATIONS	$N V^2 (\Delta n)^2$	$\frac{1}{(1+Q^2 l_c^2)^2}$	$\frac{1}{Q^{-4}}$
LINE DISLOCATIONS	$\frac{\rho}{V_A} a_{coh}^2 b^2 \frac{\pi}{2} \left(\frac{1-2\nu}{1-\nu} \right)^2$	$\frac{G(Q R_0)}{Q^{-3}}$	$\frac{1}{Q^{-3}}$
MULTIPLE REFRACTION	\exp	$-\frac{\epsilon^2}{\beta n \lambda^4 n^2}$	

N = density of scatterers, V = scatterer volume, l_c = correlation length, ρ = dislocation density, b = Burgers vector, ν = Poisson ration, V_A = atomic volume, G = interference function, η = number of refractions, n = differential neutron scattering length, $\epsilon = 2\theta$ = scattering angle.

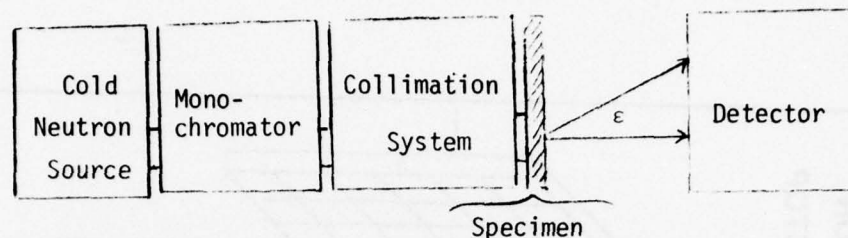
the particle volume, V , is known, the surface area can be determined. The difficulty is that the normalization integral must be evaluated between zero and infinity in Q , while the experimental data covers only a small part of this range. Extending the integrand to the upper limit can be done analytically since the high angle part of the experimental data depends on Q^{-4} . However, extrapolating the data to zero angle is a more uncertain procedure, and, hence, there will always be some uncertainty as to the accuracy of the results.

We have so far discussed methods of determining the radius of gyration, shape, volume and surface area of the heterogeneities from the form of the scattering curve, without absolute intensity measurements. If absolute measurements are carried out, the molecular weight can also be determined, provided the concentration of the solution, the chemical composition and the density of solute and solvent are known and if there is no internal hydration. In all these cases, the scattering curve has to be corrected for interparticle interference effects prior to analysis.

The above methods of analysis have been applied to the study of shape, size, and distribution of precipitates in metallic systems, in particular, GP zones in age-hardened aluminum alloys (39). The distribution of the zones is polydisperse, and interparticle interference effects predominate. Hence, the computed results always have to be treated with caution. The same must be noted for much of the applied work that follows.

4. Experimental Arrangements

The main elements of a SANS system include:



The major source of neutrons is the steady state reactor (other sources were discussed in Sec. IIB). Table VIII shows the luminosity of x-rays and neutron sources, and it is seen that the high flux ILL-Grenoble and BNL reactors are lower by orders of magnitude than x-ray sources available today. There are, however, good reasons to use neutrons, as will be seen presently.

In any case, cold neutrons are obtained by moderation in a refrigerator and exit through an opening in the reactor vessel. Collimation is carried out by absorption at slits or through critical scattering by polished surfaces, or both. Monochromatization is achieved by crystal reflection, critical reflection and by mechanical selection (1,2).

The scattered beam is detected by a modified film method, counter or an area detector. The scattered intensity is registered and analyzed by the appropriate integration of computer hardware.

Fig. 6 shows a typical experimental arrangement for SANS. It is essentially the ILL-Grenoble setup, and is the basis for the Herald AWRE and Brookhaven facilities (BNL currently uses this arrangement for a SANS facility dedicated mainly to biology experiments. In addition, monochromatization is achieved by a newly developed multi-layer monochromator - to be discussed later (48)).

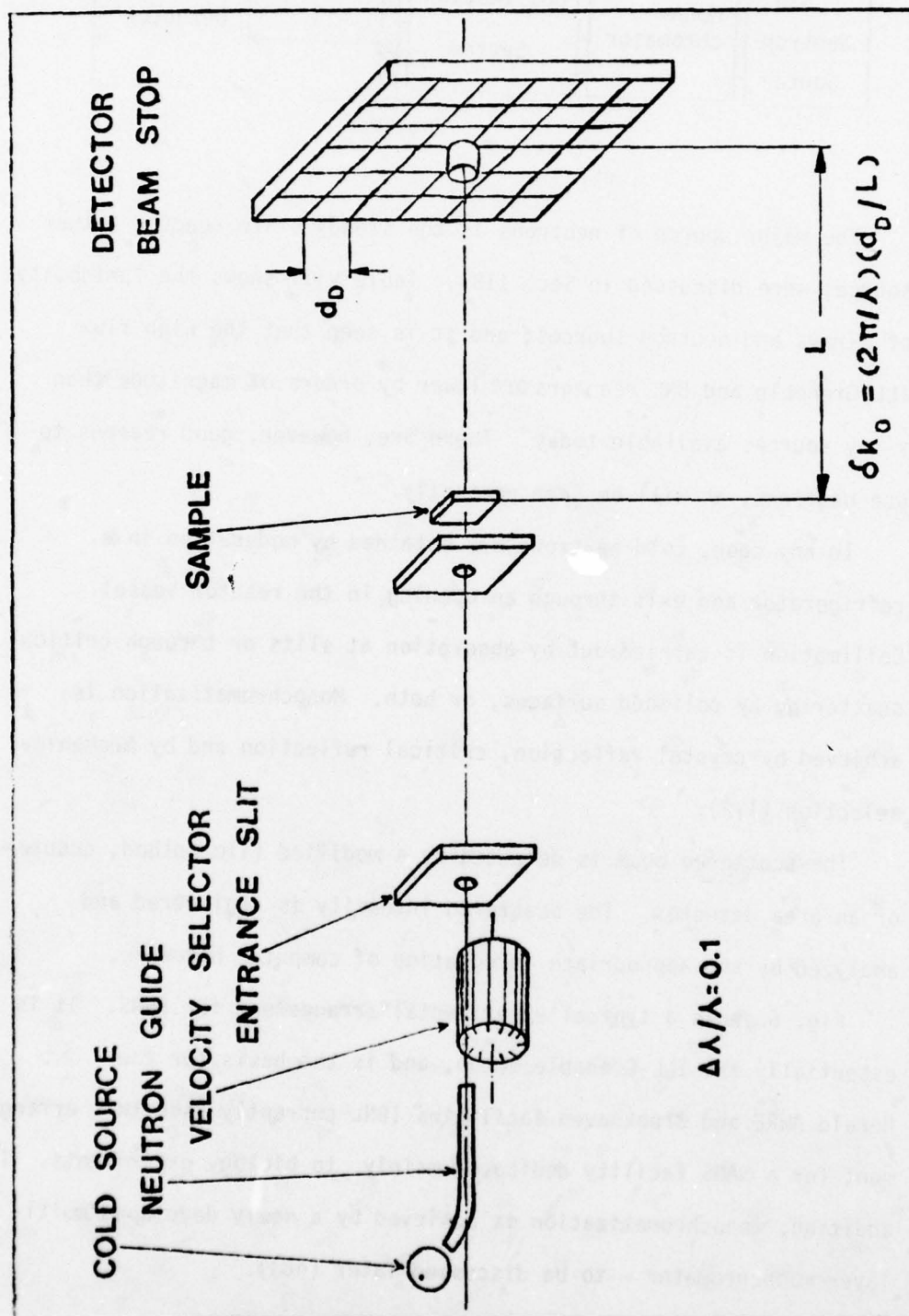


Fig. 6 Schematic of prototype small-angle neutron scattering facility.

TABLE VIII

Luminosity of X-Ray and Neutron Sources with $\Delta\lambda/\lambda = 0.5 \times 10^{-3}$ (After Schmatz).

Source	Sterad ⁻¹ Cm ⁻² sec ⁻¹
Rotating Anode 100 KW	10^{17} photons
Conventional X-Ray Source Fixed Anode	10^{15} photons
Synchrotron (DESY)	10^{19} photons
Reactor-Medium Flux Munich (6 \AA Neutrons)	10^7 neutrons
Reactor-High Flux ILL and BNL (6 \AA Neutrons)	10^{10} neutrons

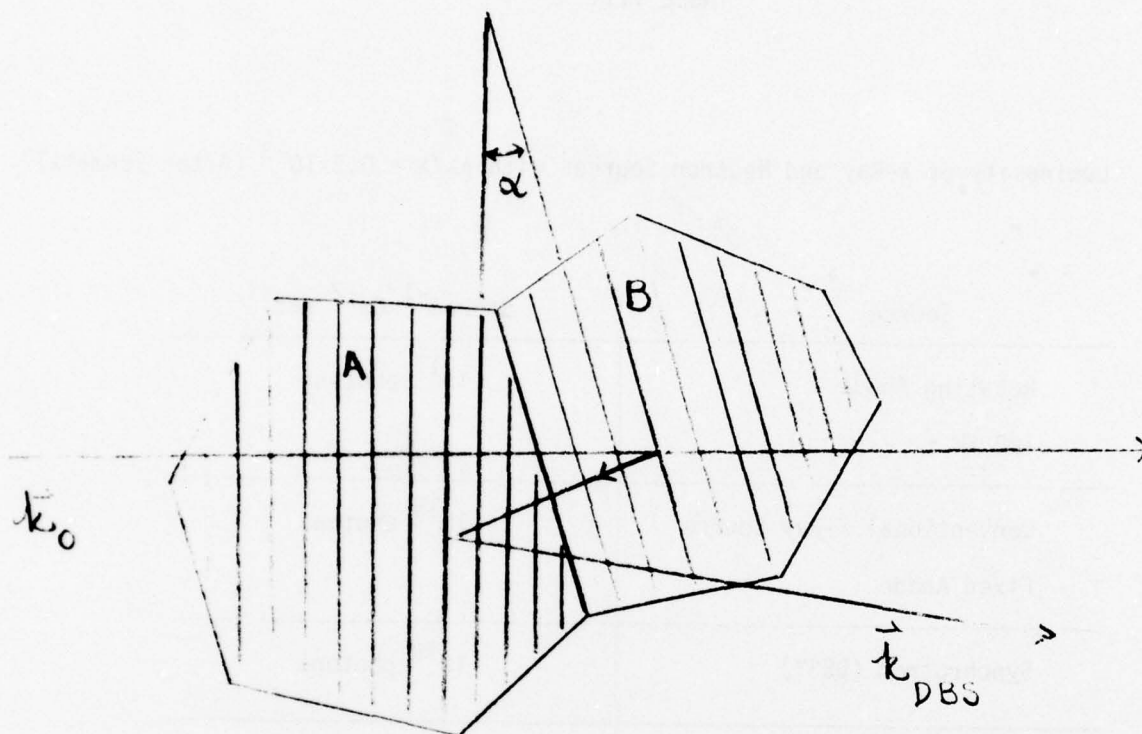


Fig. 7

Schematic representation of double-Bragg scattering. Crystallites A and B are at a slight angle, α , to one-another. \vec{k}_0 is the incident beam and \vec{k}_{DBS} is the beam that has undergone multiple scattering (Ref. 40).

a. Double-Bragg Scattering (DBS)

If the SANS intensity is Bragg diffracted within a crystal, and an adjacent portion of the grain is at a slight angle to the original diffracting plane, then that primary ray can again be reflected, emerging at some distance away from the direct beam: Fig. 7. Thus, plastic deformation, which gives significant mosaic spread, can result in measurable double-Bragg scattering. This scattering, especially for weakly scattering systems, represents a parasitic background and will tend to confuse the scattered profile (1,2,30,36,40). DBS can be avoided by using neutrons of wavelengths at least twice that of the largest lattice spacing within the crystal. Thus, if for a cubic crystal the lattice parameter is 4 \AA , one must use at least 8 \AA neutrons to avoid DBS: Hence, the need for cold sources for applied studies.

b. Monochromators for Low-Energy Neutrons

The usual problem encountered in diffraction experiments is angular resolution-versus-intensity. This is particularly true for SANS, where the systems under consideration are weakly scattering, while a high degree of resolution is required. Much experience at European laboratories has enabled practical solutions, and it is possible to devise relatively simple small-angle scattering set-ups to handle reactor beams.

i. Guide Tubes

The optimum arrangement uses a beam tube of such a cross-section geometry so as to yield minimum divergence, yet

to give sufficient intensity of sub-thermal neutrons from the cold source. This is accomplished by taking advantage of the principle of the total reflection of neutrons which occurs at a critical glancing angle, given by

$$\theta_c = \lambda \sqrt{Nb/\pi} \quad (16)$$

where λ is the neutron wavelength, N is the density (nuclei/cm³) of nuclei of scattering length b for the material making up the inner surface of the guide tube. (Generally, $N\bar{b}$ is employed and is considered to be equal to $\sum N_r \bar{b}_r$, the summation being taken over all the types of nuclei which are present, where N_r is the nuclear density for the r th nucleus. \bar{b} is the average value of the bound coherent scattering amplitude.)

The reflectivity varies with glancing angle according to Fig. 8

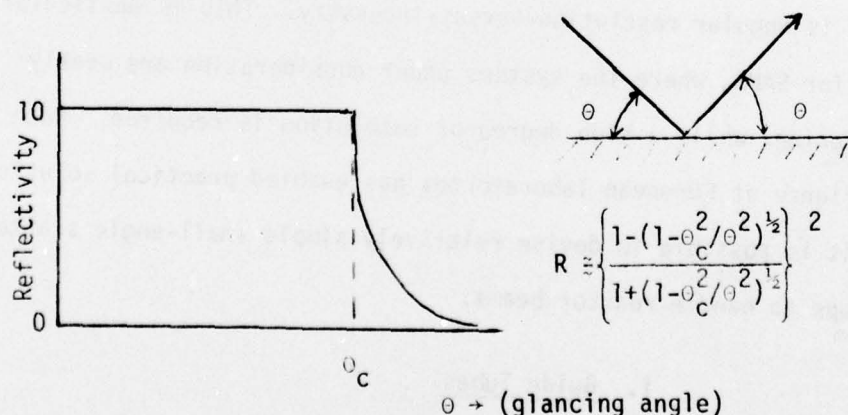


Fig. 8 - Reflectivity plotted versus glancing angle near the critical reflection, calculated according to the indicated equation for $R = f(\theta)$, for a critical glancing angle of $10'$ (After Bacon, Chapter 5, Ref. 1).

It is obvious from Fig. 8 and the equation for R that by controlling the maximum angle of divergence (i.e., the beam tube diameter) it is possible to achieve a wavelength cut-off below which the reflectivity is zero. In fact, most neutron collimators for SANS are designed with this principle in mind.

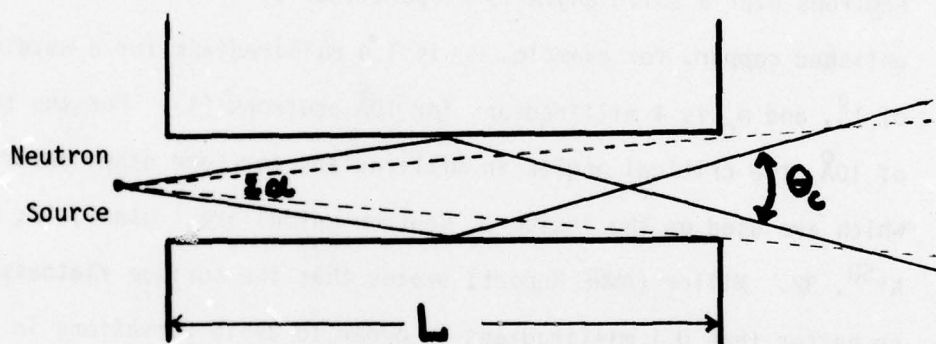


Fig. 9 - Schematic of the way in which total internal reflection with a collimating tube can increase the beam's angular divergence beyond that specified by that for L/a . (After Bacon, Chapter 5, Ref. 1).

In Fig. 9, $\pm \alpha$ denotes the maximum divergence which will increase with the ratio $(a/L)^2$, for a square cross-section. When the internal surfaces are total reflecting at a glancing angle θ_c , the collimation angle must be less than $\pm \theta_c$. The beam intensity will thus be increased by internal reflection, but divergence will be increased to a solid angle of $4\theta_c^2$.

An important aspect of using total internal reflection is that the beam of neutrons can be transported with little loss for a long distance from the reactor face. Thus, though divergence is increased, the background γ from the reactor is substantially decreased. Furthermore, by increasing the value of L , one obtains increased collimation. The overall effect of an internal reflecting guide versus a non-reflecting guide yields a gain of $(4\theta_c^2)(L/a)^2$. It was seen from Eq. (16) that θ_c and λ are proportional. Therefore, the flux of neutrons over a solid angle is proportional to λ^2 . For the case of polished copper, for example, θ_c is 1.4 milliradians for a wavelength of 1\AA , and θ_c is 4 milliradians for 10\AA neutrons (1). For the case of 10\AA , the critical angles in milliradians for some other materials which are used on the inside of neutron guides are: glass, 12; Ni, 17; Ni⁵⁸, 32. Miller (AWRE Report) states that the surface flatness must be better than 0.1 milliradians in order to avoid variations in incident angle. This can, of course, be achieved for glasses; and Cu and Ni have been evaporated on glass (2). For neutron scattering, typical collimation angles are in the range 0.5 - 1.0 degree. Therefore, the critical angles, in the range of collimation angle, only really apply for long wavelength neutrons.

In order to remove the lower range of wavelengths, long guide tube are highly effective. For example, Schmatz has shown that for $\lambda > 3\text{\AA}$, the diverging solid angles are equal for (i) a monochromating crystal 5 meters away from the core and (ii) a guide tube with a natural nickel internal surface. Furthermore, the guide tubes can be bent, which has the dual effect of i) increasing the angle of incidence, further removing shorter wavelengths (high pass filtration),

and ii) removing a line-of-sight view of the reactor core from the emerging end of the guide tube (1,2,36). Thus, γ -rays and fast neutrons are removed, with the result of a substantially decreased parasitic background at the detector. To remove line-of-sight problems, the tube, with an internal natural nickel surface, is bent to a radius R_c , given by

$$R_c[\text{meters}] = 1.38 \times 10^4 A[\text{cm}] (\lambda_{\text{opt}}[\text{\AA}]^{-2}) \quad (17)$$

where, for a square cross-section, A is a side, and λ_{opt} is the optimum wavelength. The minimum length for avoiding line-of-sight is

$$L_{\text{min}} = 2(2 R_c A)^{\frac{1}{2}} \quad (18)$$

For $A = 3$ cm and for wavelengths from 2\AA to 20\AA , R_c ranges from 10,300 to 103 meters and L_{min} is between 49 and 4.9 meters (2, 49-53).

Schmatz states (2) that, based on experience, the transmission factors can be 80% for long wavelengths. (Although, higher values have been reported to me by British and French workers; i.e., approaching 90% for carefully prepared internal surfaces.) The ILL reactor has perhaps the most advanced "user-oriented" guide tube arrangement. Ten tubes exiting from the reactor enter the experiment hall, where perhaps 20 instruments are served. The guide tubes yield a range of wavelengths. For example:

λ [\AA]	R [meters] (radius of curvature)	L [meters] (length of guide tube)
0.88	27,000	90
2.8	2,700	30
29	25	10

Specifically, long neutron guide tubes, of rectangular cross-section, internally glass-plated with nickel, are operational at a number of European facilities: FRM, Munich (50); EL3, Saclay (51); FRJ-2, Jülich (53); HFR, ILL-Grenoble (52).

For more modest constructions, circular tubes, shorter in length than described above, are used. For long wavelengths, these set-ups are considerably cheaper and can be almost as efficient.

ii. Beam Filters

A further removal of the low wavelength side of the spectrum can be achieved through the use of beam filters. For example, if a beryllium polycrystal is placed in the beam path, all wavelengths below $\sim 4\text{\AA}$ will be Bragg reflected out of the neutron beam. The beryllium thus acts as a high-pass filter. The efficiency of the beam filter can be significantly enhanced by cooling to 77°K. This lower temperature decreases lattice vibrations, and sharpens the Bragg cut-off edge. The spectral distributions of cold neutrons from a BeO beam filter is shown in Fig. 10, after Fermi and Marshall, quoted by Amaldi (54).

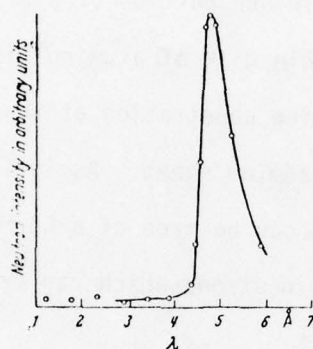


Fig. 10 Spectral distribution of cold neutrons from a beryllium oxide filter (After Fermi and Marshall, see Ref. 54).

iii. Mechanical velocity selector (MVS)

The MVS is actually a time-of-flight device, incorporating a series of rotating shutters which are phased relative to one-another such that only neutrons having a narrow band of velocities will penetrate the system. From the De Broglie relation, the neutron wavelength is related to velocity through:

$$\lambda_n = h/m_n v_n \quad (19)$$

where $(m_n v_n)$ is the momentum of the neutron. The device is pictured in Fig. 11. In the particular unit shown here (after Ringo, Ref. 55)

the slots are helical, and neutrons of a given velocity range are thus guided from the beam tube. In actual operation, the MVS can be comprised of sets of rotating disks made of aluminum which are covered by cadmium, except in one portion of a disk. The cadmium is very absorbing, while the thin disk of aluminum is essentially transparent to neutrons, permitting penetration at that sector of the disk not covered with the cadmium sheet. As indicated previously, the neutron absorbing vanes can be made of a Cd-Mg alloy.

The velocity, v , of the neutrons which can transverse the rotating MVS is

$$v = L_M \omega / \Phi \quad (20)$$

where L_M is the length of the MVS, ω is the angular velocity and Φ is the phase change which the neutron wave experiences between the entrance and exit sectors of the monochromator. The approximate velocity resolution is given by:

$$\begin{aligned} \Delta v &= \Delta \phi v^2 / \omega r \\ \text{or} \\ v / \Delta v &= (\omega r / \Delta \phi v) \end{aligned} \quad (21)$$

where $\Delta \phi$ is the angular spread of the neutron beam at the entrance slit, and in the direction of the moving entrance slit, and r is the radius of the MVS. For thermal neutrons ($v \approx 2 \times 10^5$) the velocity resolution is 0.1, which is as good as the angular resolution ($1/\Delta \phi$). Since this sort of resolution is poor for diffraction-type studies, the MVS is not particularly desirable. However, for lower velocities

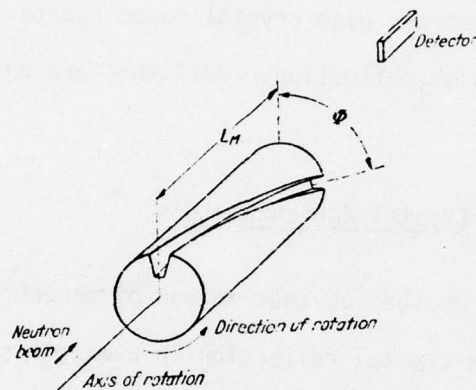


Fig. 11 Mechanical Velocity Selector (Ref. 54).

(i.e., for longer wavelength neutrons) the velocity resolution, and thus the wavelength resolution, increases, and the MVS becomes useful as a device for neutron monochromatization. The advantages of MVS for long wavelength neutrons over crystal monochromators are simplicity and the avoidance of high reflection orders that are encountered with crystals.

iv. Crystal Monochromators

Another obvious method of monochromatizing the neutron beam is to use crystal reflection in a manner similar to that employed in x-ray diffraction (1,38). The crystal in question may be used either in reflection or in transmission. With a quality crystal, selected appropriately to Bragg-reflect the correct wavelength, up to 60% efficiency can be obtained. Generally, large crystals of beryllium, copper and germanium are employed. Again, just as for x-rays, the monochromating efficiency will depend on the quality of the crystal and on the degree of collimation. It is commonly possible to obtain wavelength resolution of around 4%.

One difficulty with the use of crystals for monochromatizing long wavelength neutrons (e.g., $\lambda_n > 5 \text{ \AA}$) is the occurrence of orders of reflections. For this reason, as well as for simplicity of alignment, MVS is generally employed for SANS, as was discussed above.

v. Multilayer Monochromators

A more recent development in this field (especially for SANS) is due to workers at Brookhaven National Laboratory's HFBR. Schoenborn and co-workers have fabricated thin-film monochromators for neutrons. This approach is aimed specifically at applications

in the realm of small angles. These workers have also demonstrated that this thin-film device can be used as efficient neutron polarizers and filters (56,57).

The method of making the Schoenborn monochromator is to alternately deposit thin films of two different materials. By adjusting the spacings of these films, the multilayer monochromator can be constructed with a neutron reflective efficiency comparable with pyrolytic graphite crystals. Furthermore, the spacings can be varied, thus effectively tuning the monochromator to the needs of a particular experiment.

For choice of the film materials, it is necessary that there be a large difference in their respective neutron-scattering amplitude densities. The larger the difference, the greater will be the neutron intensity. The materials should also be capable of being formed into a good thin film, and there should be limited interdiffusion. It is imperative that the thicknesses of all layers be equal to within a few percent.

Schoenborn and co-workers, based on the above considerations, have constructed a multilayer monochromator of manganese and germanium. This monochromator was fabricated by vacuum deposition (10^{-6} Torr) of 75 bilayers, having a periodicity of 200 \AA .

Kinematical theory can be used to predict that the multilayer monochromator acts effectively to channel radiation by a process of highly efficient repetitive reflections, yielding a net reflectivity approaching 90%. Furthermore, due to the inherently small take-off angle and some aperiodicity in the spacings, the bandwidth, $\Delta\lambda/\lambda$, for the initially constructed multilayers is large and reasonably adjustable.

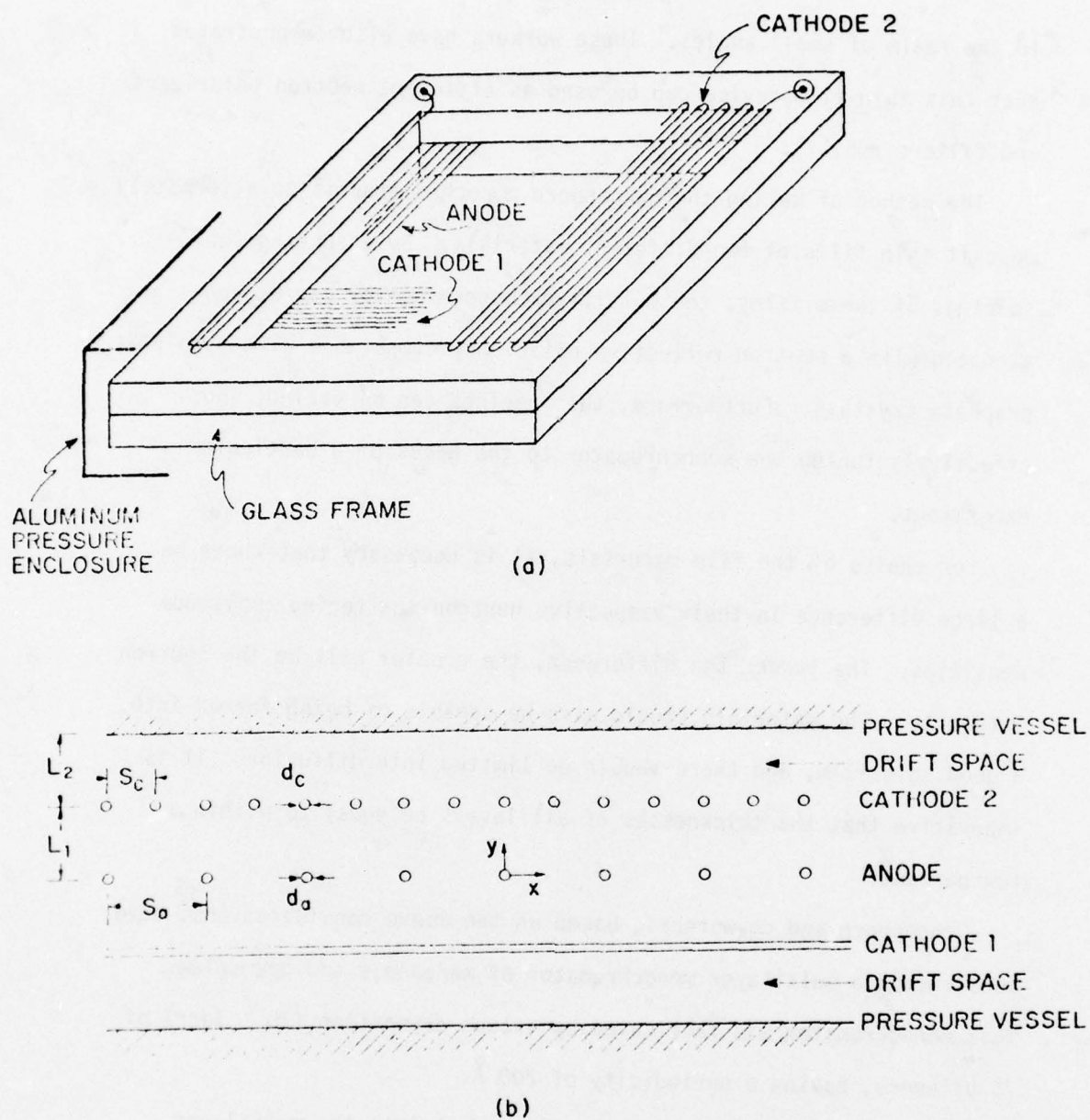


Fig. 12 Area detector schematic; proposed for Brookhaven National Laboratory SANS facility (See Table III and specifications given below.)

Since intensity is frequently of great importance in SANS, it is believed by this writer that the large $\Delta\lambda/\lambda$ can be accepted due to the resulting attendant increase in intensity. Indeed, aside from the MVS, the multilayer monochromator represents a highly efficient monochromator for long wavelength neutrons from a cold source.

c. Area Detectors

The need to use two-dimensional detectors has been described above. Generally, anisotropic effects are important to detect in solids, especially for technological studies (e.g., texture, oriented precipitates, directional composites). Furthermore, the new area detectors give superior resolution when compared with point counting and linear detectors (30-32, 36, 48).

The detector gas (either BF_3 or pressurized He^3) is contained within an thin-walled aluminum disk. The system is threaded with anode and cathode wires, laid-down at right angles to one another. The BNL area detector is shown schematically in Fig. 12. The scattered neutron generates a gamma which causes ionization. The breakdown is detected between adjacent anode-cathode pairs and a pulse is sent to the adder. The geometric resolution of this system is determined by the grid spacing. For example, FIAT uses a multicellular BF_3 propositional counter with 64x64 array (i.e., 4096 cells with a cross-section of 1 cm x 1 cm). The amplified signals which emanate from the area detector, are binary coded according to their cell origin (x,y position) and transferred to a computer, where they are accumulated. It is possible to monitor the scattering experiment dynamically in a visual mode. The FIAT area detector was obtained from CEA-CENG, Grenoble,

France (36).

Given below are the specifications for a proposed SANS multi-detector and control system for HFBR at Brookhaven National Laboratory (58).

Detector and Control System for a Small Angle Neutron Spectrometer

Detector

An area sensitive neutron detector is proposed with the following approximate specifications:

Wave length of neutrons: $\sim 8\text{\AA}$;
Maximum random counting rate: $\sim 10^4$;
Sensitive area: $\sim 20 \times 20 \text{ cm}^2$ nominal;
Spatial resolution: $\sim 3\text{mm}$ FWHM in horizontal and vertical directions;
Container: single volume pressure vessel with external purifier and circulating pump;
Gas: $\text{He}^3 + \text{A} + \text{CH}_4$ or CO_2 ;
Window thickness: $3/8"$ aluminum for 10 atm.;
Readout: Charge division readout in both dimensions.

Data Acquisition and Control System

A multiprocessor system is proposed which has the following components:

- Data Memory: It is proposed to sort the incoming data in real time in random access memory. Core or semiconducting memory of 128K x 16 bit is provided. 32K x 32 bits are used for a real time data array into which events can be sorted randomly in approximately 6 μsec per event.
- Data Input: A special purpose processor will obtain the event from the two ADC's, one 8-bit for the X-axis and one 7-bit for the Y-axis, calculate the appropriate addresses and sort (increment) the event into the data memory.
- Main Control: The FORTRAN written Application Programs will be executed at the Main Control computer node. They may consist of up to 62 overlays. Approximately 1 million words will be available for on-line storage of programs. Approximately 1 million words will be available for temporary data storage. Experiment data will be recorded on magnetic tape. A PDP11/34 will be used as a processor.
- On-line Display: A real-time display system with an independent LS111 processor will allow the generation of displays on CRT while data is collected. The display

programs do not influence or disturb in any way the data collection process. The display programs will be coded in FORTRAN. An initial set of programs will be provided.

Program Development: The RECF Program Development Node will be used for editing, compiling and linking of FORTRAN application programs.

A significant portion of the non-commercial hardware and software of the above referenced system components have been developed in the past years within the BNL RECF project and within the H3-Spectrometer project. Estimates in time and cost, therefore, refer to expansions, construction, system integration and tests. The Motor Control System, which is referenced below, will be developed because it is uneconomical to apply the old designs which are presently used at the HFBR.

Motor Control: The specifications of the motor control system depend on the mechanical specifications of the spectrometer. The mechanical specifications are not yet fully determined. The following should, therefore, be considered a preliminary approach. It is intended to use a stepping motor and an optical absolute shaft encoder with a 5-digit BCD output (0 to 36,000) for each axis to be controlled. Three axis are assumed to be controlled.

B. Applications

In the following sections will be given an overview of the ways in which SANS has been employed to study technological materials and to perform NDE on alloys-in-use. Metallurgically, the fine, coherent GP zones received much attention with both x-ray and neutron small-angle scattering. Much experience in the areas has enabled us to proceed to more complex situations in materials, and, specifically, cold neutron SANS is permitting us to study plastically deformed alloys.

We shall first examine precipitation systems and then consider the more complex cases.

1. Thermal Treatments

Thermomechanical and precipitation strengthening heat treatment of a wide range of ferrous as well as non-ferrous alloys represent excellent candidates for studies using SANS. The very earliest application of SAXS to metallurgy was due to Guinier and Preston (e.g., Ref. 39), who independently detected and characterized the early-stage decomposition product of aging of supersaturated Al-base Cu solid solution. Following rapid quenching from the solid solution region into the two-phase region of the equilibrium phase diagram, the solute atoms (e.g., Cu for Al- 4 wt% Cu alloy) will cluster into disks parallel to and coherent with {100} planes of the aluminum parent matrix. These "Guinier-Preston Zones" (GP zones) give rise to a diffuse scattering around all of the nodes of reciprocal space and, ideally, appear as diffuse shoulders on the normal lattice Bragg reflections. However, it is best to study this scattering at the center of reciprocal space (i.e., at 0,0,0) since there is no competitive Bragg peak here and, also, the strain effects which modify any scattering process essentially disappear.

The shortcoming of using x-rays for studies of solid state precipitation has been the limited techniques of analysis that are available to transform the scattering profiles into meaningful structural information. Also, the absorption of x-rays is high and only very thin specimens can generally be employed (e.g., ~ 0.003 inch for aluminum alloys). Furthermore, in order to detect clusters of atoms using SAXS, it is required that their respective atomic numbers

differ considerably. This is because, for x-rays, the extra-nuclear electrons are responsible for scattering and at small angles, the intensity of the x-rays scattered by a cluster will be proportional to the square of the difference in electron density, or the square of the differential atomic number. If that number is small (e.g., Si or Mg in Al; which are important alloying constituents in aluminum alloys) there will be essentially no scattered intensity due to the solute cluster.

Neutrons scatter with strengths related in no continuous fashion to atomic number (See Fig. 4). Thus, though Al and Mg are adjacent to each other on the period table their coherent scattering cross-sections for neutrons differ sufficiently to yield intensity from coherent clusters of magnesium within an aluminum matrix, and permit determination of the size and density.

Further, the neutrons can traverse a thicker specimen than can be studied with the usually-employed x-rays of the order of 1 \AA wavelength. Of particular importance, as discussed above, neutrons can be sufficiently slowed down to yield long wavelengths of values beyond the Bragg cut-off, and these neutrons do not undergo double-Bragg scattering.

SANS is ideally suited for studies of precipitation of finely dispersed second-phase particles; e.g., GP zones. The zones are the major strengthening constituent in aluminum alloys as well as in the maraging stainless steels. The particle density of these essentially coherent particles is high (ranging between 10^{16} and 10^{18} cm^{-3}) and their composition differs considerably from that of the matrix. Their scattering ability will in principle be good, making such a system

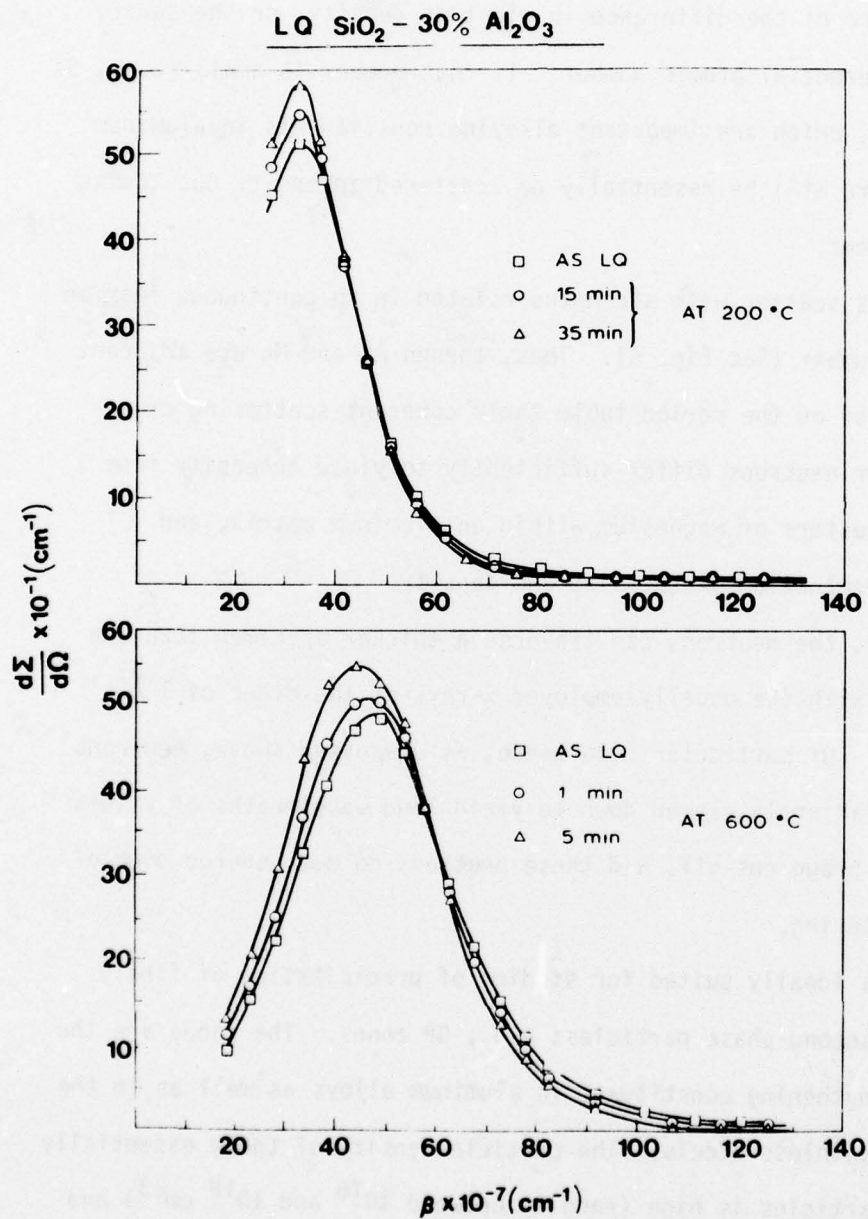


Fig. 13

Differential scattering cross-section plotted versus scattering angle for aging at 200°C and 600°C.

highly suitable for small-angle scattering studies. In fact, much work has gone into characterizing such systems using SAXS, and, more recently, SANS is finding important application as well.

A fair number of scientifically oriented SANS experiments have been carried out on alloy and ceramic systems which show clustering. These have been performed in the main by workers at ILL-Grenoble and at KFA-Jülich. Some systems which have been studied are discussed below.

a. Amorphous SiO_2 - 30% Al_2O_3 (Silica-Mullite) (59)

This ceramic was roller-cast at high rates and annealed at different temperatures to follow the spinodal decomposition of the clustered solution. The evolution of the scattering spectrum is shown in Fig. 13 for aging at two different temperatures. A peak in scattered intensity develops with time, with only a slight shift occurring to lower angles. The presence of the intensity maximum indicates that significant interparticle interference is occurring. This has, in fact, been verified by TEM, where it is observed that the two phases are mutually interconnected. This, of course, will yield a complex scattering profile: But of central interest here is that the spacing, as determined by SANS and TEM are both about 200 Å.

b. Pt - 40% Au (60)

This alloy cannot be studied with SAXS due to the close proximity of the atomic scattering factors. SANS enters here as a powerful technique for studying precipitation. The phase diagram is shown in Fig. 14. It can be seen that the alloy in question has a

very narrow range of solid solubility region at around 1200°C, extending between the top of the miscibility gap and the solidus. This alloy has been solutionized and quenched. In addition, a specimen has actually been quenched rapidly from the liquid state at rates exceeding 10^6 °C/sec (splat cooled).

The area detector at ILL-D11A can show the evolution of the scattering profiles in two-dimensions, so that any developing anisotropy can be detected. In fact, in the present case, whether the alloy has been quenched from the solid or liquid state, it still has a fine-grained structure; but certainly, it will be much finer-grained for liquid quenching (the average grain diameter is of the order of one micron).

The area detector output of two specimens, liquid quenched and aged, and solid quenched and aged, are shown in Fig. 15a and 15b, respectively. Fig. 15a is for the solid quenched alloy, where significant anisotropy is seen. Fig. 15b, for the ultra-fine grained liquid-quenched specimen shows a pattern which is fairly isotropic.

This result is significant in that we are able to see anisotropic growth of a second phase in a polycrystalline specimen. The aligned precipitates (believed to be coherent with {100} planes of the matrix) reflect, through the two-dimensional SANS output, the recrystallization texture of the alloy plate that has been solid quenched. We thus suggest that here is a potential technique for following thermomechanical fabrication programs for alloys. This might be especially interesting for magnetic steels, for examples, since the neutron has spin and will respond to a state of magnetization within the alloy. Again, the key to studies of these kinds is the use of a two-dimensional detector.

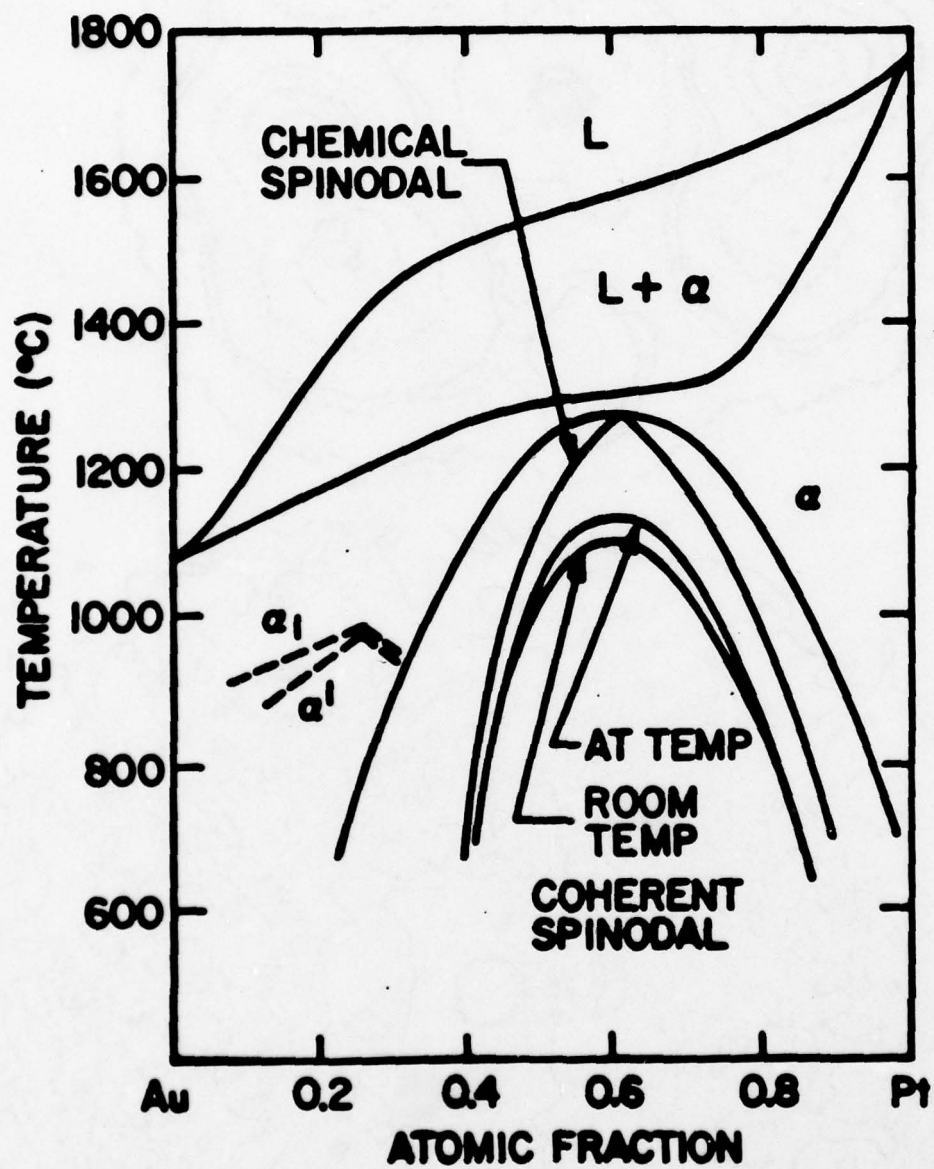


Fig. 14 Phase diagram for Au-Pt alloy system.

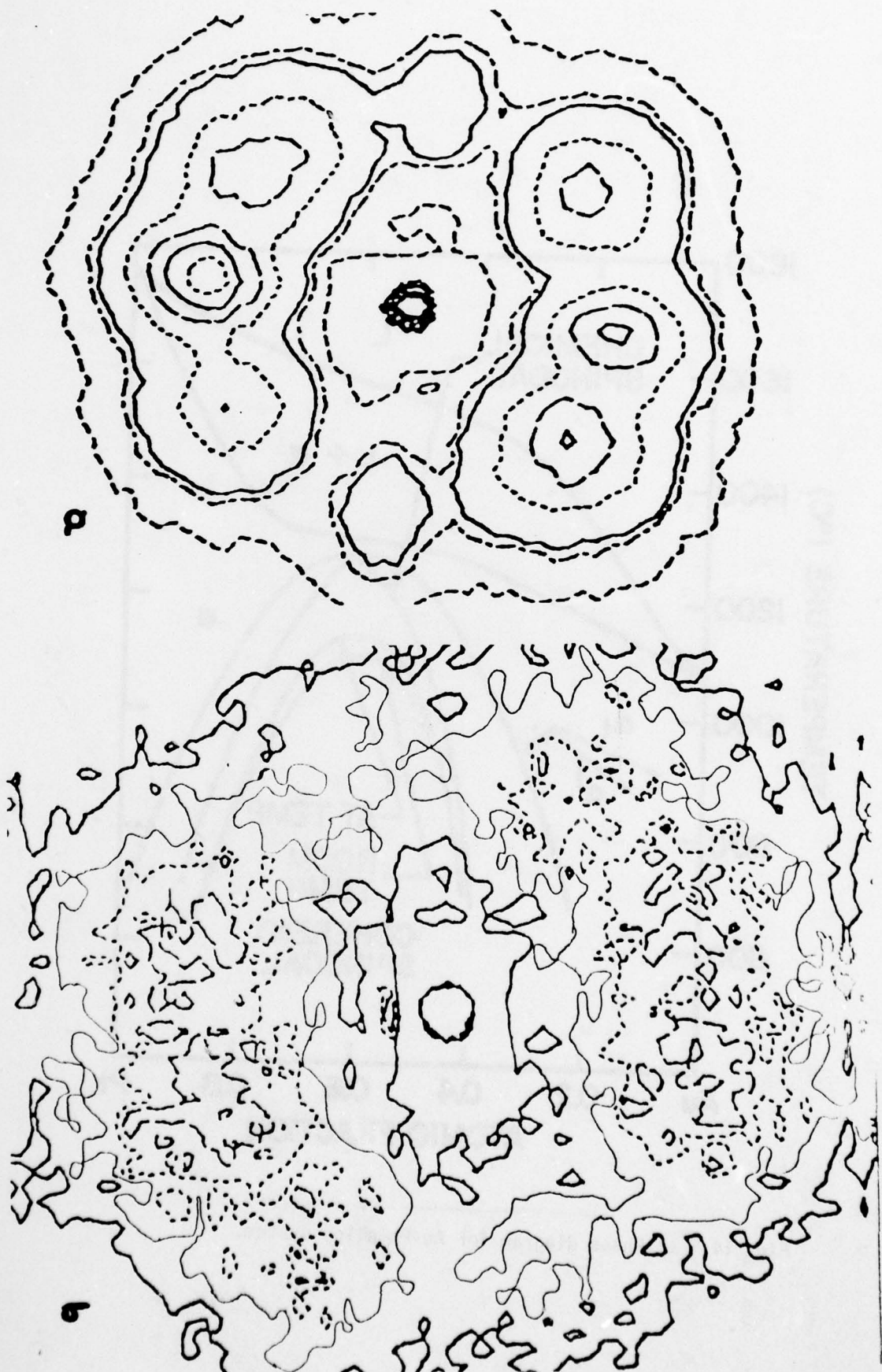
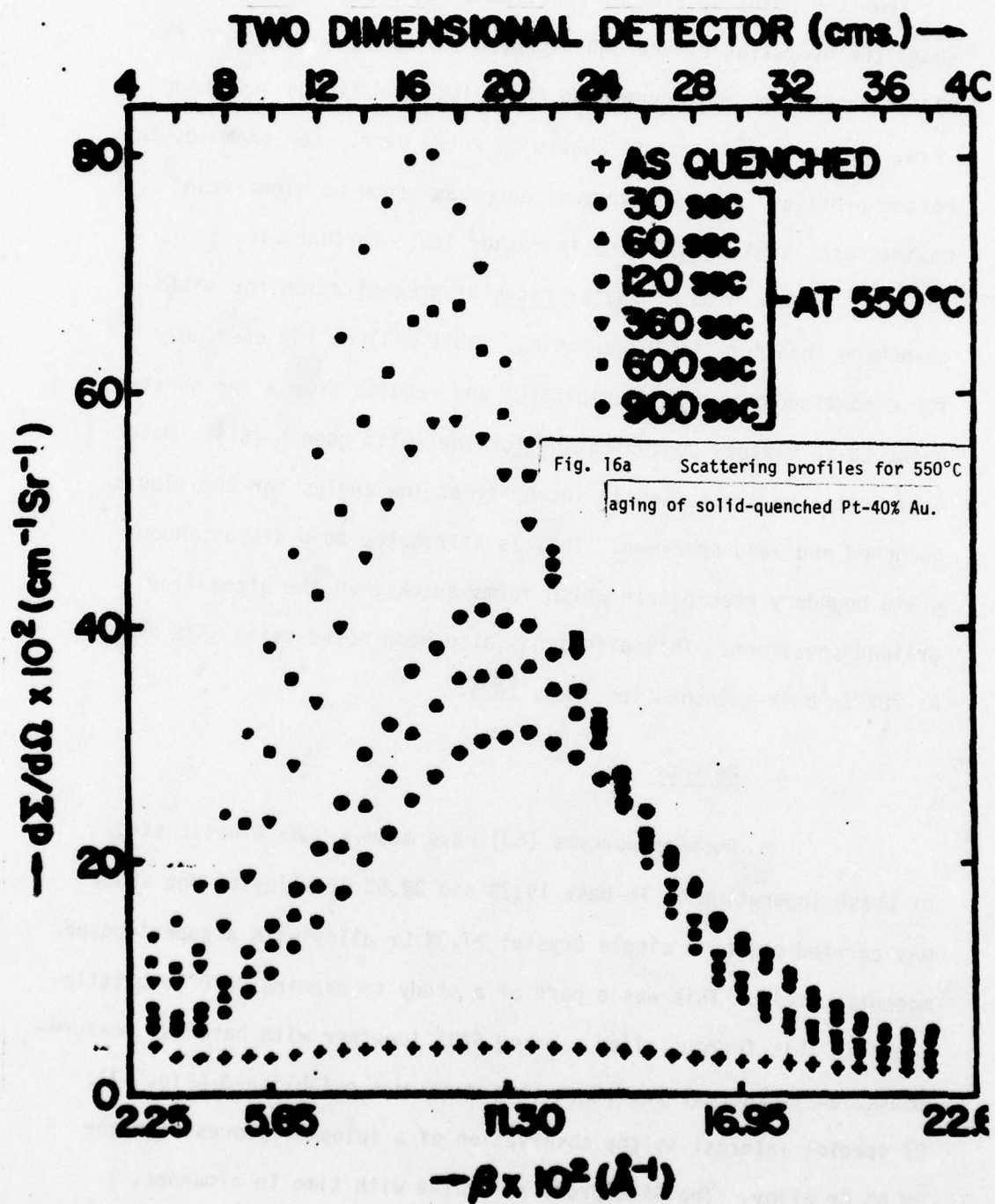


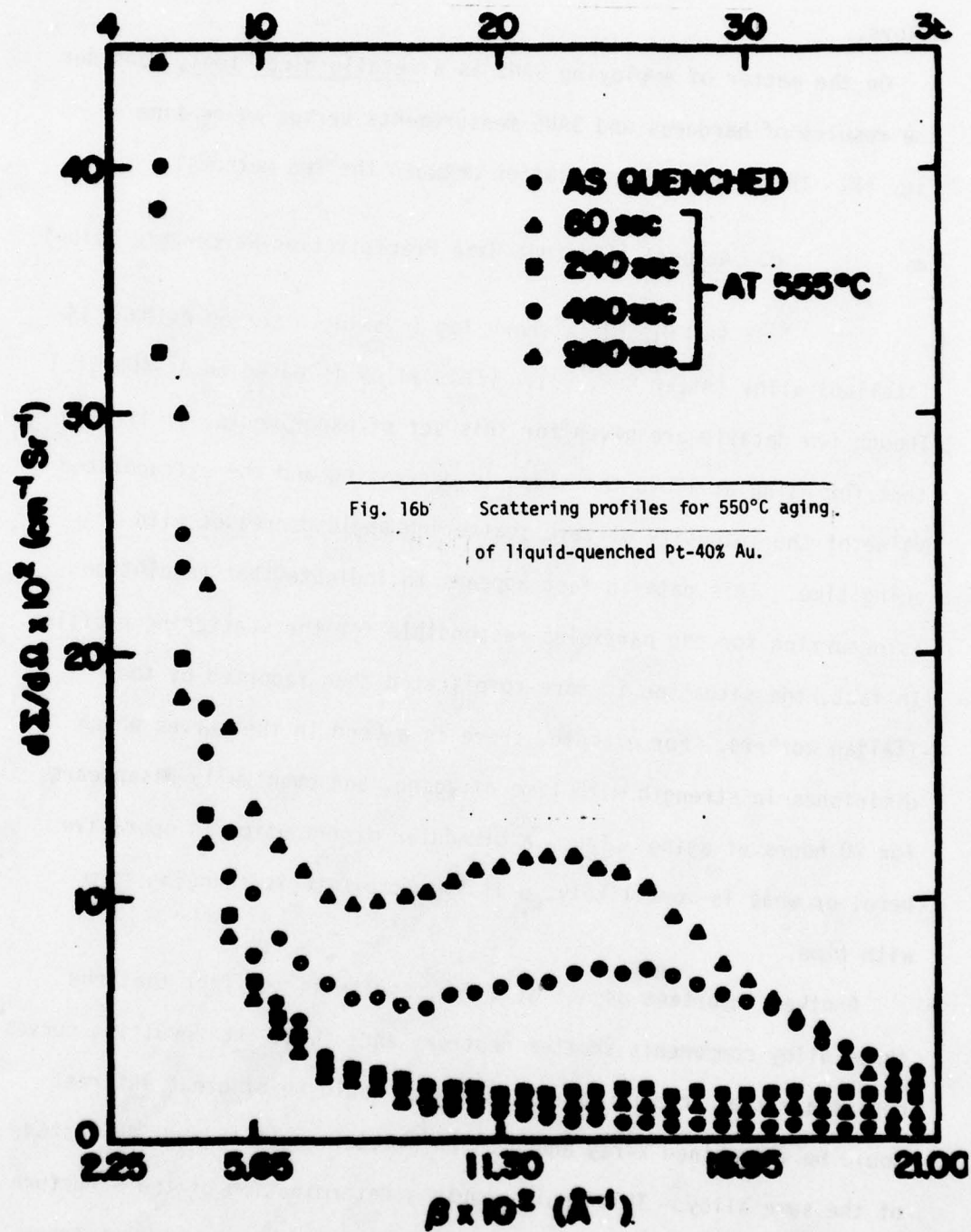
Fig. 15 Two-Dimensional output of area detector of D11 for aging Pt-40% Au alloy a) solid quench; b) liquid quenched.

From the point of view of kinetics of decomposition, Fig. 16 shows the evolution of the SANS spectra during aging at 550°C for alloys following solid quenching (Fig. 16a) and liquid quenching (Fig. 16b). Several points should be noted here. For example, the bottom profiles for both types of quenches show no significant maxima, and, thus, clustering is rather low. Furthermore, it is possible to obtain much greater rates of precipitation for solid quenching than for liquid quenching. This will be the case only for a continuous matrix precipitate and results from a far greater quenched-in vacancy concentration for the solid quench (61). Note especially the great rise in intensity at low angles for the liquid-quenched and aged specimen. This is attributed to a discontinuous grain boundary precipitate which forms quickly in the ultra-fine grained specimens. This affect has also been noted using SAXS in Al-28% Zn bulk-quenched specimens (62).

c. Fe - Cr

Russian workers (63) have made a SANS kinetic study of phase separation in Fe-base 19.7% and 39.6% Cr alloys. One study was carried out on a single crystal 27.3% Cr alloy with a superimposed magnetic field. This was a part of a study to examine "470° embrittlement" in this ferrous alloy. Using SANS together with hardness measurements, an isothermal transformation curve was established (Fig. 17). Of special interest is the observation of a spinodal process for the 39.6% Cr alloy. The SANS profiles evolve with time in a manner, I believe, which satisfies spinodal criteria. Though the approach taken by these workers may be viewed as naive, it is clear that this study assists in the understanding of spinodal process in ferrous





alloys.

On the matter of employing SANS as a metallurgical tool, consider the results of hardness and SANS measurements versus aging time - Fig. 18. There is good correlation between the two methods.

d. Avional (Aluminum-Base Precipitation-Hardenable Alloy)

In Fig. 19 is shown $\log I$ -vs- $\log \theta$ for an AVIONAL 14 (Italian) alloy (After Ref. 64). [This alloy is based on Al-4Cu-Si.] Though few details are given for this set of experiments, it is seen that for aging at 175°C the slope is decreasing and the extrapolated value of the intensity at zero scattering angle decreases with aging time. This data in fact appears to indicate that resolution is occurring for the particles responsible for the scattering profiles. In fact, the situation is more complicated than reported by the Italian workers. For example, there is a bend in the curves which diminishes in strength with time of aging, and eventually disappears for 20 hours of aging. Thus, a bimodal distribution is operative here, or what is more likely, a flat precipitate is changing form with time.

Another important aspect of these results is the fact that the three alloy components scatter neutrons and, thus, the resulting curves depict a rather complex situation. What would be of great interest would be a combined x-ray and neutron scattering (SAXS and SANS) study of the same alloy. This would enable a determination of the structure and composition of the second phase. Also, using x-rays and neutrons, one could study the effects of deformation on precipitation kinetics and the resulting microstructure.

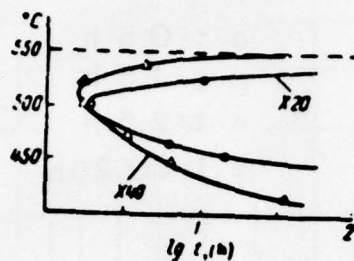
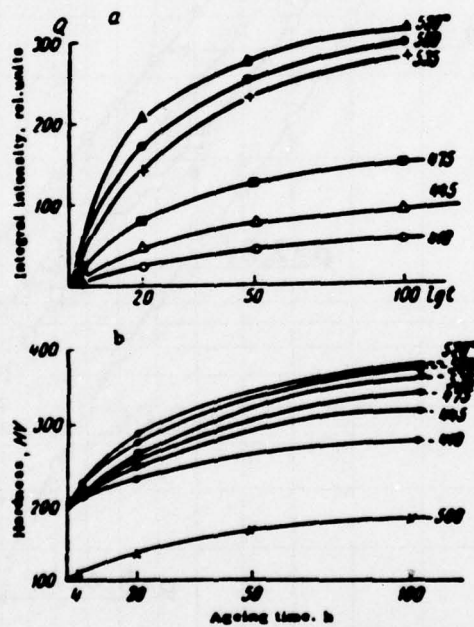
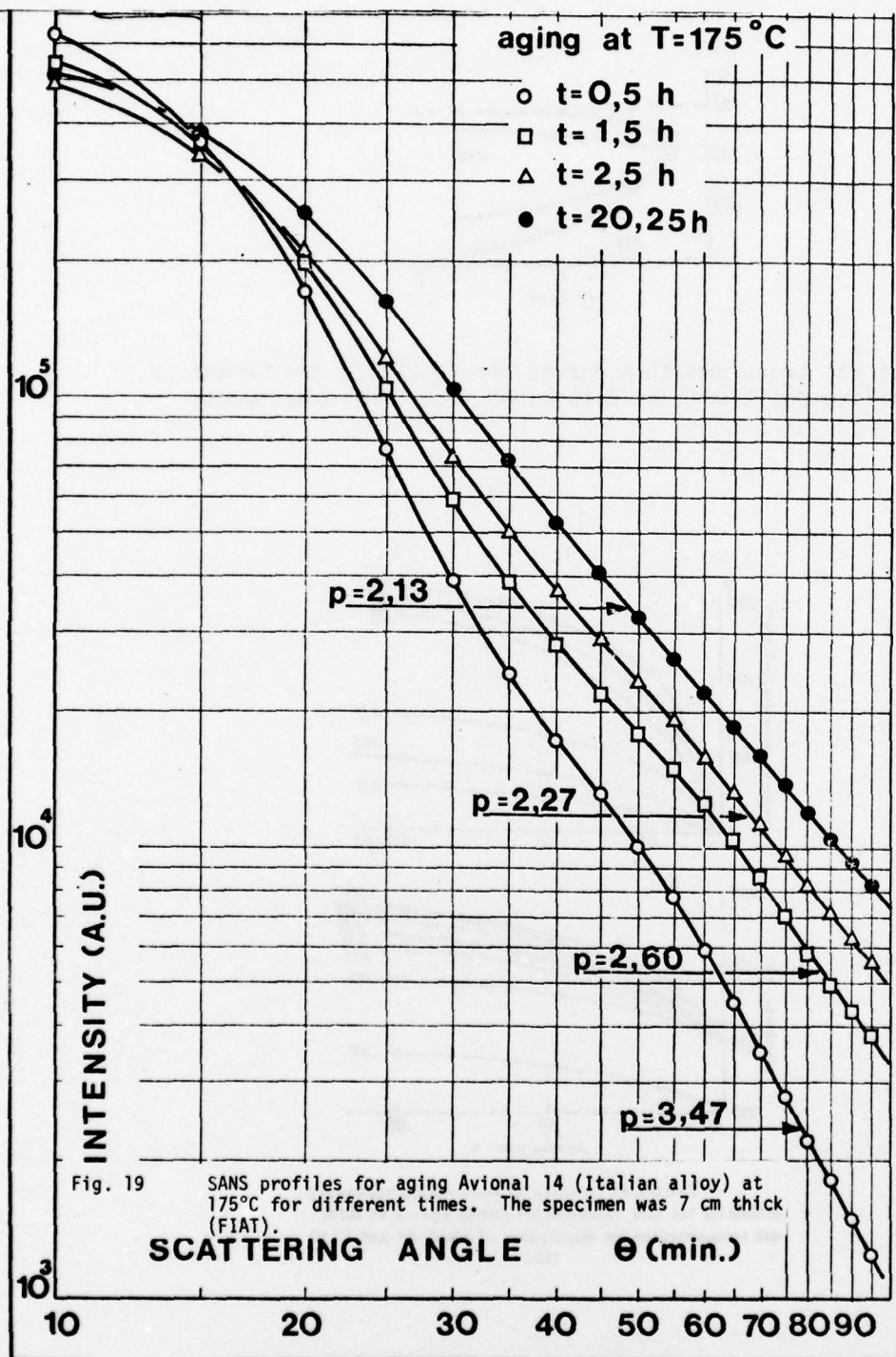


Fig. 17 Isothermal transformation curves for Fe-20% Cr and Fe-40% Cr, nominal compositions, as determined from SANS experiments (Ref. 63).



Variations in integral small-angle scattering intensity (a) and hardness (b) during ageing at different temperatures for specimens of Kh40 (●) and Kh20 (x).

Fig. 18 Integrated SANS intensity (a) and hardness (b) versus aging time for aging at different temperatures for Fe-20% Cr and Fe-40% Cr, nominal compositions (Ref. 63).



2. Commercial Alloys

The only really notable work that can be found in the literature on actual technological alloys has been done by the FIAT group (36,64-75). Though there has been considerable interest on the part of U.K. and German workers, clearly the FIAT group has pioneered in this field.

In the following are given a number of examples, due mainly to FIAT, of SANS studies of engineering alloys. These include ferrous alloys and nickel-base superalloys. Also considered by these workers has been creep and fatigue. Of special interest is the comparative examination of alloys with both TEM and SANS. The comparison of particle size and density is good for these two methods, further supporting the case of the utilization of SANS for NDE.

It should again be noted that the Italian workers are limited by having a relatively low flux cold source. Therefore, both resolution and intensity must perforce suffer. Also, though they do use an area detector, they have not published two-dimensional data outputs, but only scattering profiles. We are thus uncertain as to the degree of anisotropy that develops with time, for example, in rolled sheet. The area detector is a powerful adjunct to SANS, making possible important studies that were hitherto not possible; e.g., fiber-reinforced composites.

Finally, metallurgical insight is frequently limited in a number of the published reports on applied SANS. It can only be hoped that in the future, cooperative programs will develop between neutron diffractionists and metallurgists.

a. Precipitation Strengthened Stainless Steels Maraging 17-4PH

The Italian workers have made a preliminary study of a maraging steel; specifically, 17-4 PH. The details of the kinetics and microstructure of these precipitation-hardenable stainless steels are very complex. One must contend with the simultaneous occurrence of martensite, austenite and a fine precipitate structure. SANS studies, though desirable here, are complicated by the fact that neutrons have spin and are thus scattered by magnetic domains. Actually, the neutrons suffer magnetic scattering which is superimposed on scattering due to the fine particles of the precipitate phase.

The application of a magnetic field during the scattering experiments enables the determination of the scattering profiles with and without the field and, therefore, permits one to separate out the effects due to the magnetic domains (presumably, inter-domain refraction).

The experimental set-up for scattering with a superimposed magnetic field is given in Fig. 20. The role of the magnetic field is to orient magnetic domains in a single direction and thereby to eliminate multiple refractions.

Figs. 21a and 21b show, respectively, the relative broadening due to retained austenite as detected by neutrons, and the retained austenite as seen by x-rays. The two techniques yield similar results as a function of tempering temperature. The differences that are encountered between the curves result from precipitates of the order of 100 \AA in mean radius (TEM yields the same sizes as does SANS) (64).

For studies of large magnetic structures, such as those encountered here, refraction caused by the magnetic domains - of different refractive

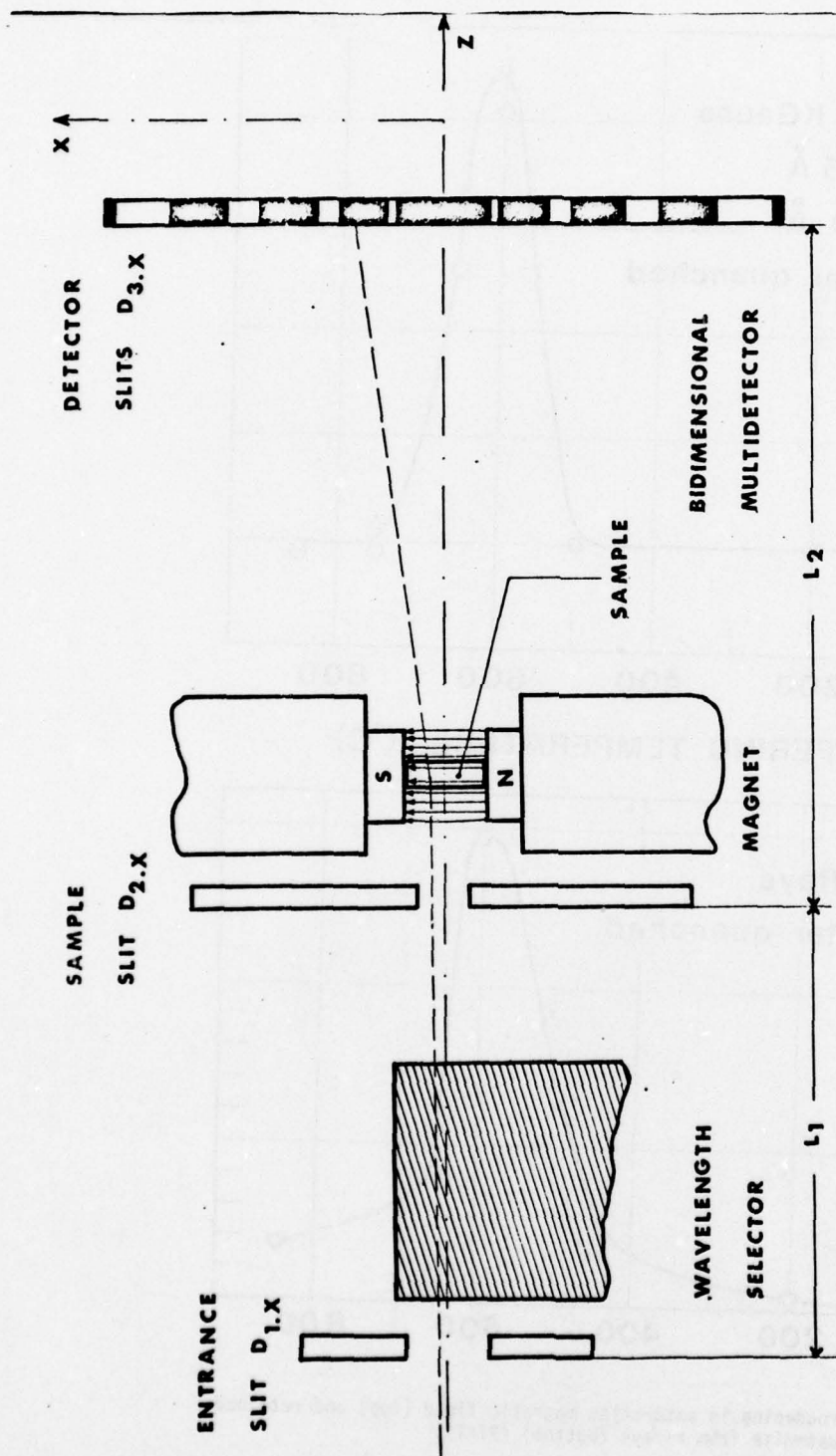


Fig. 20 FIAT SANS experimental arrangement with magnet at sample position.

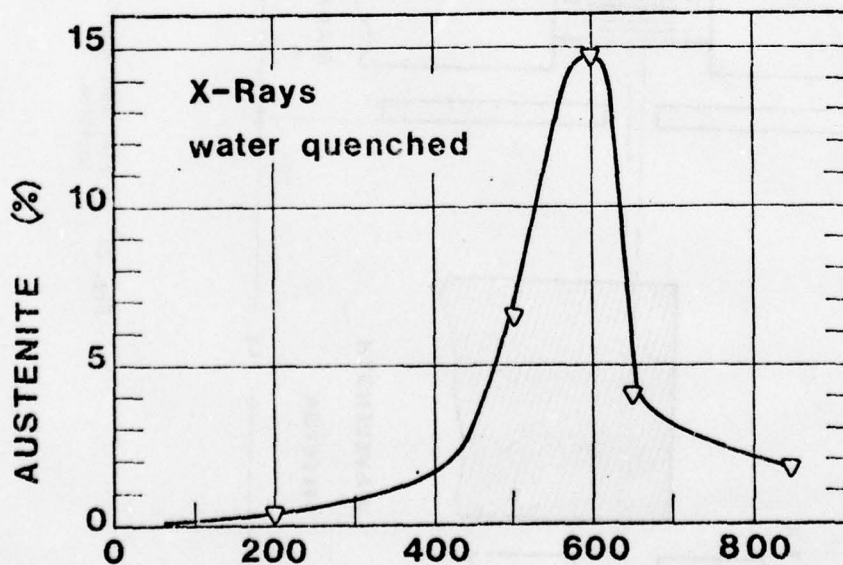
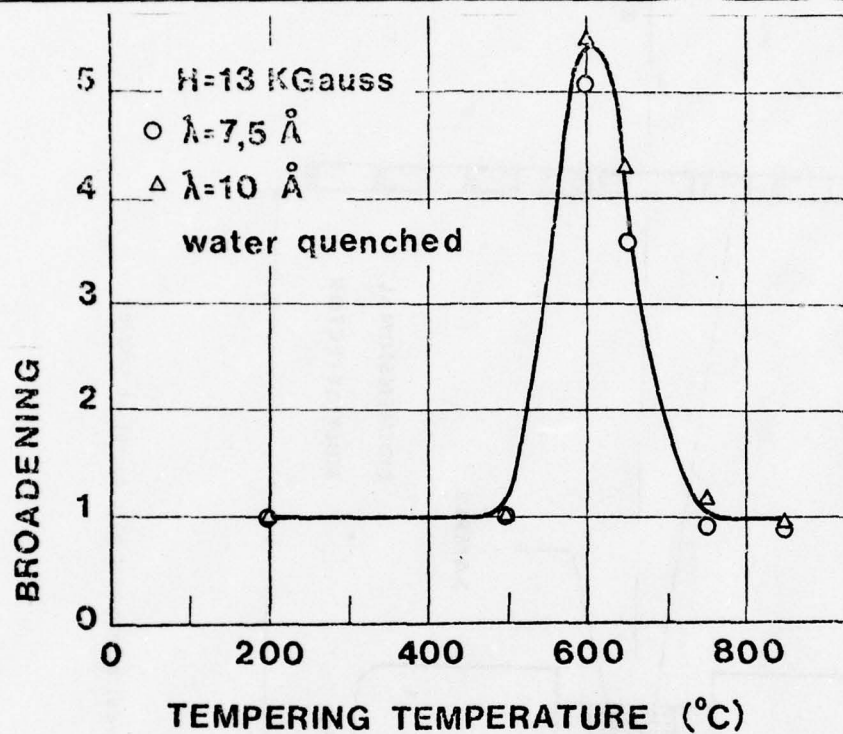


Fig. 21. Broadening in saturation magnetic field (top) and retained austenite from x-rays (bottom) (FIAT).

index - are found by the FIAT workers to be very useful. The primary beam will be broadened if it encounters material of different refractive index as it traverses the specimen (1). For beam broadening due to multiple refraction effects, the scattered intensity normally takes a Gaussian form:

$$I = I(0) \exp \left[\frac{a \cdot (2\theta)^2}{\Delta\theta^2} \right] \quad (22)$$

where $\Delta\theta^2 = n \cdot \lambda^4 \cdot \Delta\rho^2$

n = number of refractions

$\Delta\rho$ = differential scattering length densities

a = constant

Thus, the broadening varies with λ^4 .

To test the refraction concept, the FIAT workers obtained scattering curves for two different λ 's; λ_1 and λ_2 (65). The results are shown in Fig. 22, where data for two different aging temperatures are shown, 350°C and 425°C. To test for magnetic refraction effects, the two λ 's are used to obtain the two sets of scattering curves. It can be shown that refraction is operative when the slopes vary as $(\lambda_2/\lambda_1)^4$, whereas for Guinier scattering the slopes should vary as $(\lambda_2/\lambda_1)^2$. The former is, in fact, observed in the small angle regime, whereas, straightforward particle scattering is seen for the larger angle portion of the profiles, and this results from copper-rich precipitates. The small-angle refraction (actually, beam broadening) is here due to the magnetic domains, as discussed above.

The use of the refraction concept has not been extensive in neutron small-angle scattering. With the advent of the FIAT group's approach, however, it becomes possible to separate particle diffraction effects

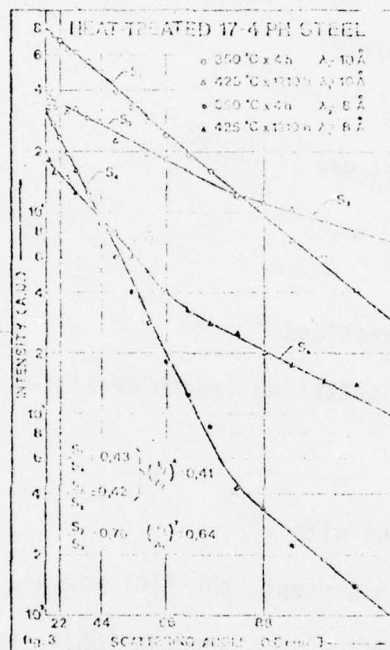


Fig. 22 Broadening analysis at two wavelengths for aging at two different temperatures for heat treated 17-4 PH steel. Log I - log ϕ plot. (Ref. 65).

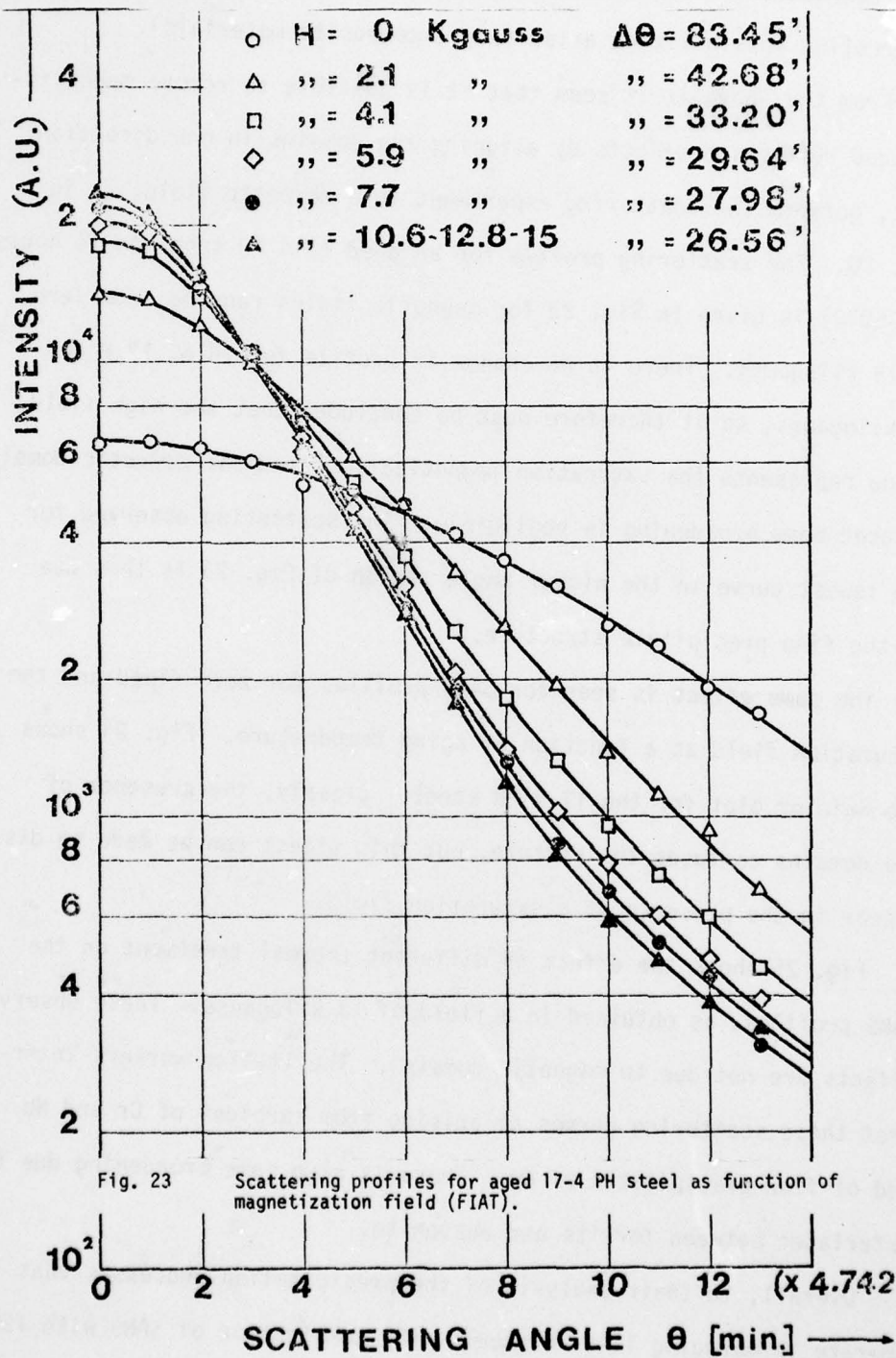
from refraction-induced beam broadening and, thus, new and rather interesting possibilities arise (e.g., composite materials).

From the above it is seen that it is possible to remove magnetic-induced refraction effects by aligning the domains in one direction; i.e., perform the scattering experiment in a magnetic field; as in Fig. 20. The scattering profile for an aged 17-4 PH specimen (4 hours at 650°C) is given in Fig. 23 for magnetic fields ranging from zero to 15 kilogauss. There is no change in profile for 10.6, 12.8 and 15 kilogauss, so it therefore must be concluded that the high field value represents the saturation magnetization, and the magnetic-domain induced beam broadening is negligible. The scattering observed for the lowest curve in the higher angle region of Fig. 23 is thus due to the fine precipitate structure.

The same effect is seen for SANS profiles for zero field and the saturation field as a function of aging temperature. Fig. 24 shows the Guinier plot for the 17.4 PH steel. Clearly, the presence of the domains confuses the picture, but this effect can be made to disappear in the presence of a saturation field.

Fig. 25 shows the effect of different thermal treatment on the SANS profiles, as obtained in a field of 13 kilogauss. These observed effects are not due to magnetic domains. The Italian workers interpret these scattering curves as arising from carbides of Cr and Nb and of fine precipitates of Cu. There is also some broadening due to interfaces between ferrite and austenite.

Overall, in their analysis of the precipitation processes that operate in maraging 17-4 PH steels, the combination of SANS with TEM gives new insight into the processes that are occurring. The prospects



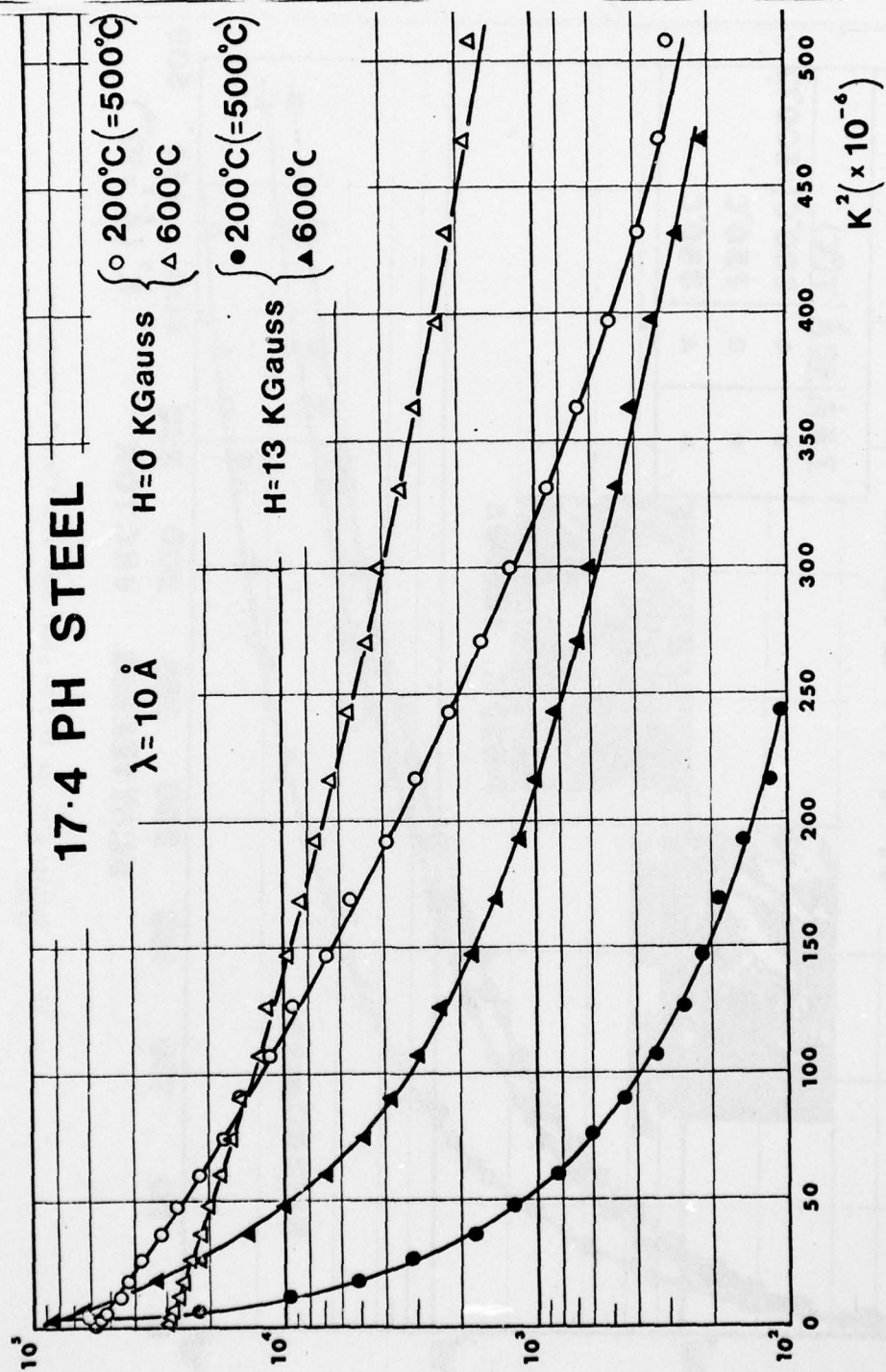


Fig. 24 Guinier plot for aged 17-4 PH steel with and without saturation field (FIAT).

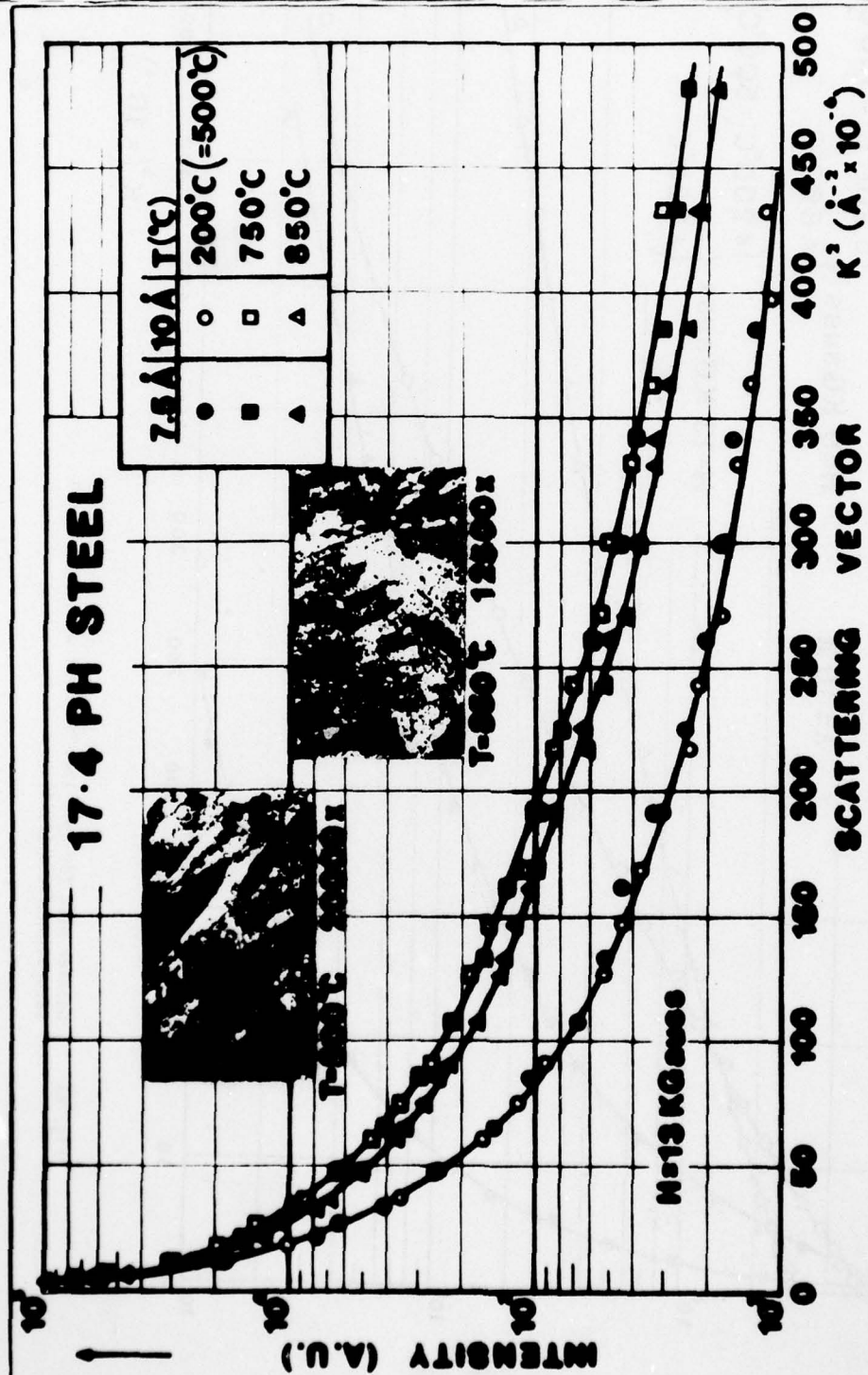


Fig. 25 Guinier plot for 17-4 PH steel aged at different temperatures (FIAT).

for this sort of approach in alloy development are exciting indeed.

b. Nickel-Base Superalloys

These alloys are designed for high temperature service; e.g., in gas turbine engines. It is essential that they have good resistance to impact damage, thermal shock and creep. The FIAT workers, in recognition of the limitation of standard NDE control of these in-service materials, have devised a series of SANS examinations which yield a good picture of "remaining effective lifetime".

The nickel-base superalloys are strengthened by a distribution of γ' particles $\text{Ni}_3(\text{Ti}, \text{Al})$ intermetallic phase] which restrict dislocation motion, both by slip and climb. The γ' phase must be stable for the alloy to maintain strength at high operating temperatures and with a superimposed creep load (for example, as turbine blades). The FIAT Laboratories have decided to examine SANS, in conjunction with TEM as a monitor, as a possible NDE method for following the evolution of the microstructure in "real" turbine blades which have been in service.

Much of what follows is data from in-service specimens, but a good deal comes from laboratory annealings and treatments. One problem is that the reports contain little detailed information. We shall thus have to make some assumptions and attempt to put a picture together of the FIAT accomplishments to date.

i. UDIMET-710

The preliminary FIAT study was concerned with the Udimet 710 alloy [Cr(17.30), Mo(3.38), Co(15.0), W(1.5), Ti(4.92), Al(2.58), B(0.015), C(0.07), Ni(55); in weight %] in three conditions:

(1) as-received; (2) after 18,000 hours in service, and; (3) retreated ("regeneration") following 6000 hours of use. SANS patterns were taken for these three conditions at two different positions: at the blade root and at the trailing edge, where higher temperatures are experienced in-service.

Results for the root zone are shown in Fig. 26, where two transmission electron micrographs are also given for specimen (1), as-received and for (3), 6,000 hours plus retreatment. Except for a larger secondary strengthening phase, the micrographs are similar. This is likewise seen in the SANS profiles, where the retreated specimen, 3, shows two distinct regions of curvature. Two size ranges are apparent for both TEM and SANS. Of central importance here is the fact that the low temperature at the root region does not give rise to much change in the SANS spectra after 18,000 hours of service, and, hence, this region of the blade is not apparently degraded. This is not the case for the high temperature trailing edge region, as observed in Fig. 27. Here, though 1 and 3 (as-received and as-retreated, respectively) are similar as for the root zone, the blade which was in service for 18,000 hours has degraded significantly. There can be seen a great deal of coursening through both TEM and SANS. TEM shows the average second-phase particle size to be over 4000 \AA and SANS gives a figure greater than 2000 \AA (this difference is due to geometric limitations of the FIAT SANS collimation system). In fact, the small-angle region (due to small precipitates) is gone for the in-service blade; and this, too, is confirmed by TEM. The TEM study shows that γ' has grown considerably and short chrome carbides are forming at grain boundaries.

The above observations, according to the FIAT workers, have been

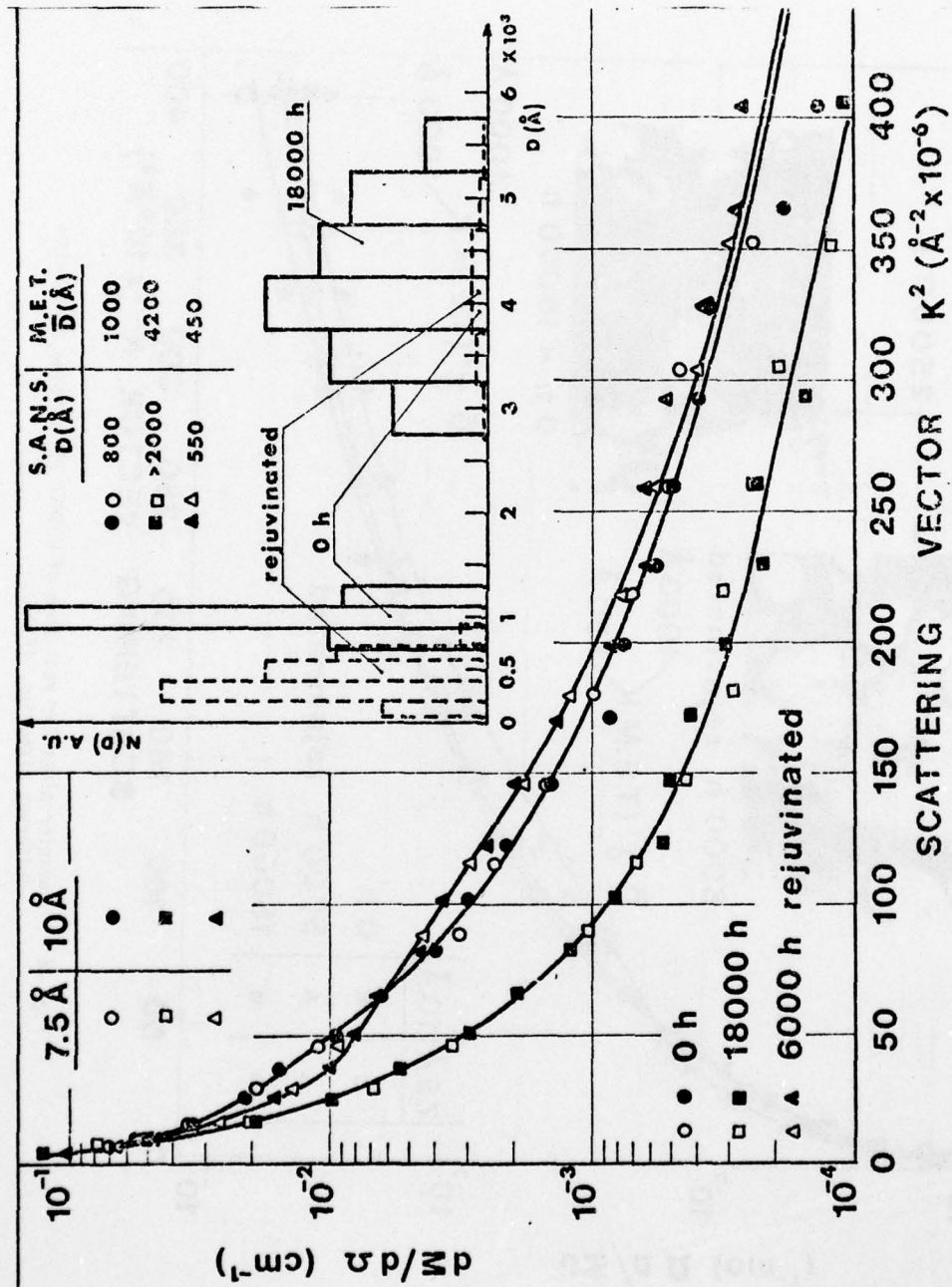


Fig. 27 Guinier plots and histograms for trailing edge of UDINET-710 turbine blade with different histories (FIAT).

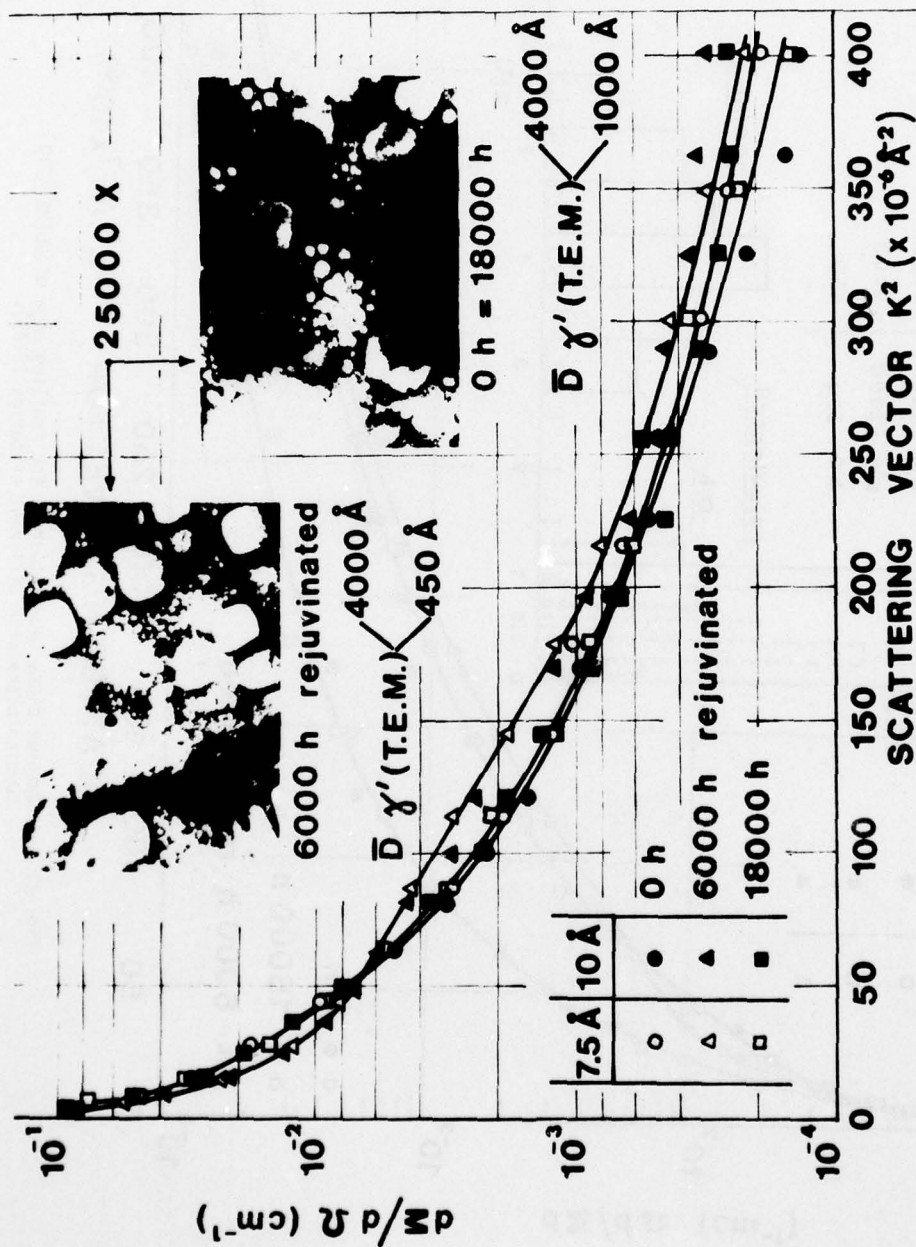


Fig. 26 Guinier plots for root zone of UDIMET-710 turbine blade with different histories. (FIAT).

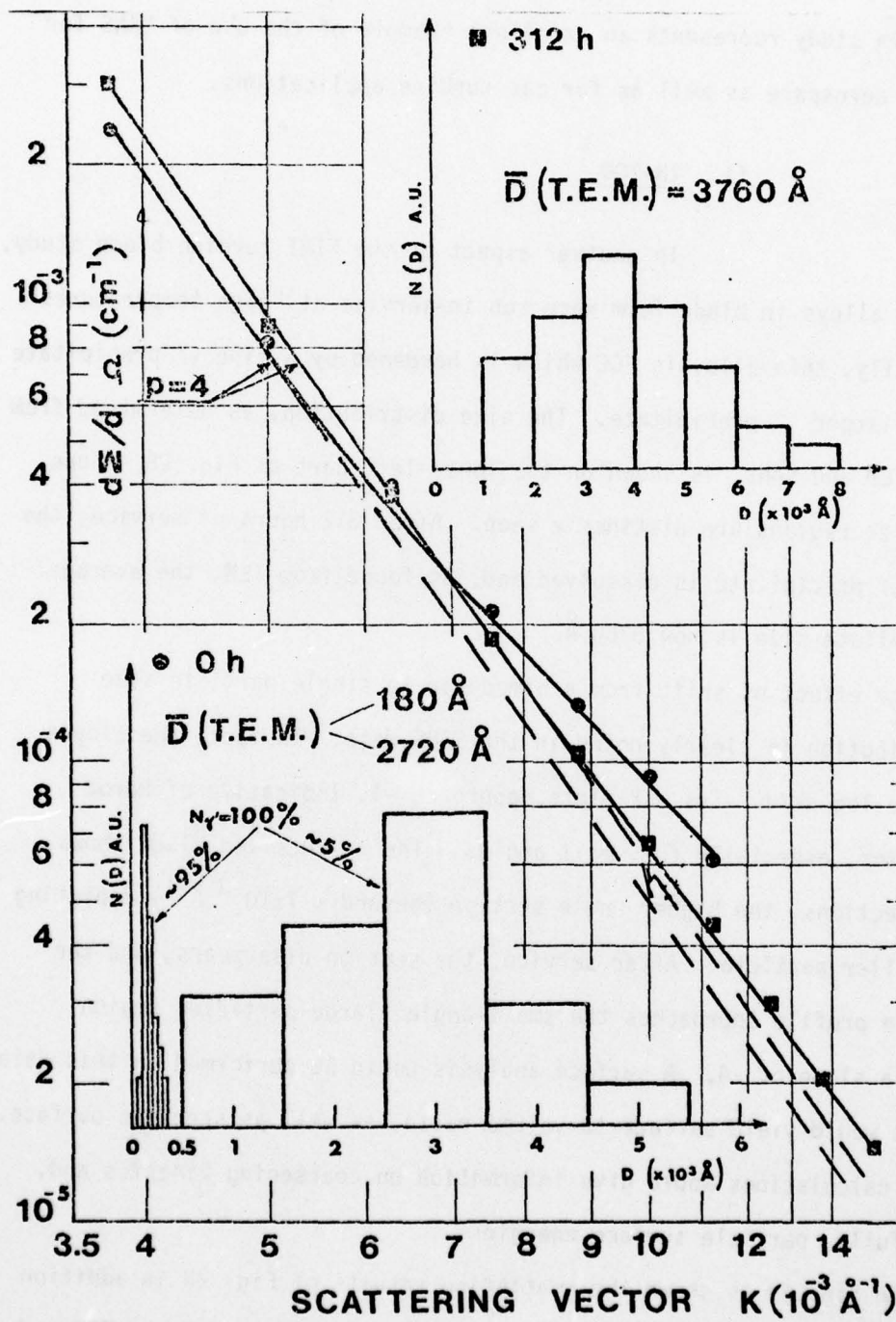


Fig. 28 Scattering profiles for IN-100 turbine blades for different thermal histories (FIAT).

confirmed by mechanical properties measurements (76).

This study represents an excellent example of the use of SANS for NDE in aerospace as well as for gas turbine applications.

ii. IN-100

In another aspect of the FIAT turbine blade study, IN-100 alloys in blade form were run in-service at "high temperatures". Generally, this alloy is FCC which is hardened by a fine γ' precipitate and a larger γ' precipitate. The size distribution, as determined from both TEM and SANS, is shown on the lower-left part of Fig. 28, where two size regions are distinctly seen. After 312 hours of service, the smaller precipitate is dissolved and, as found from TEM, the average precipitate size is now 3760 Å.

The effect of shift from a bimodal to single particle size distribution is clearly noted in the SANS data. In fact, the slopes of the $\log d\Sigma/d\Omega$ - vs - K plots, approach -4, indicative of Porod behavior, especially for small angles. The as-received blade shows two sections, the higher angle section (beyond $\sim 7 \times 10^{-3} \text{ Å}^{-1}$) depicting a smaller particle. After service, the section disappears, and the entire profile approaches the small-angle (large particle) region, with a slope of -4. A surface analysis could be performed on this data which would yield surface-to-volume ratio, as well as specific surface. Such calculations would give information on coarsening kinetics and, hopefully, particle surface energies.

In Fig. 29 is shown the scattering results of Fig. 28 in addition to TEM photos. Further confirmation of the agreement between TEM and SANS is seen from Fig. 30, where γ' particle density and size is plotted

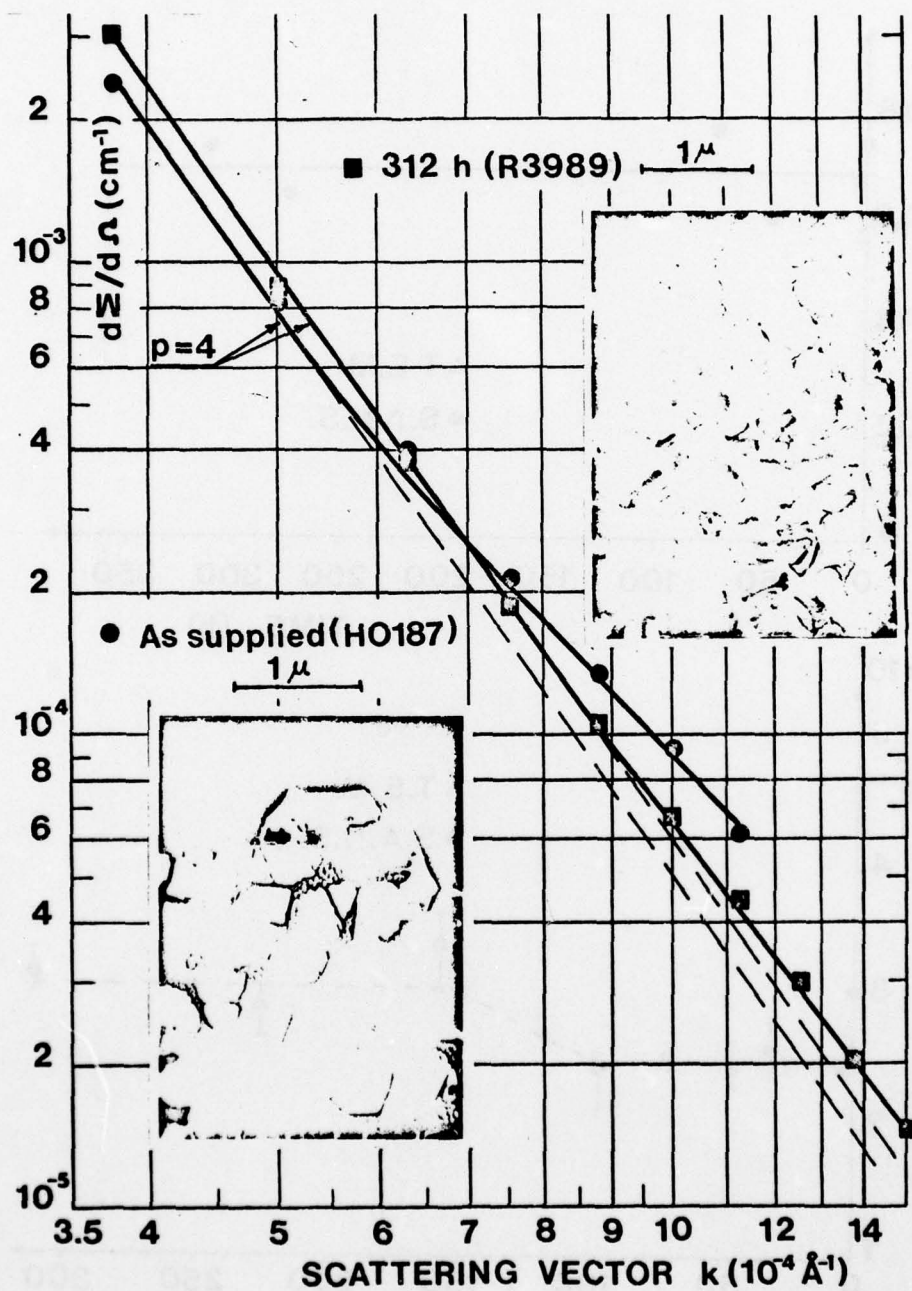


Fig. 29 Same as Fig. 28, but showing micrographs (FIAT).

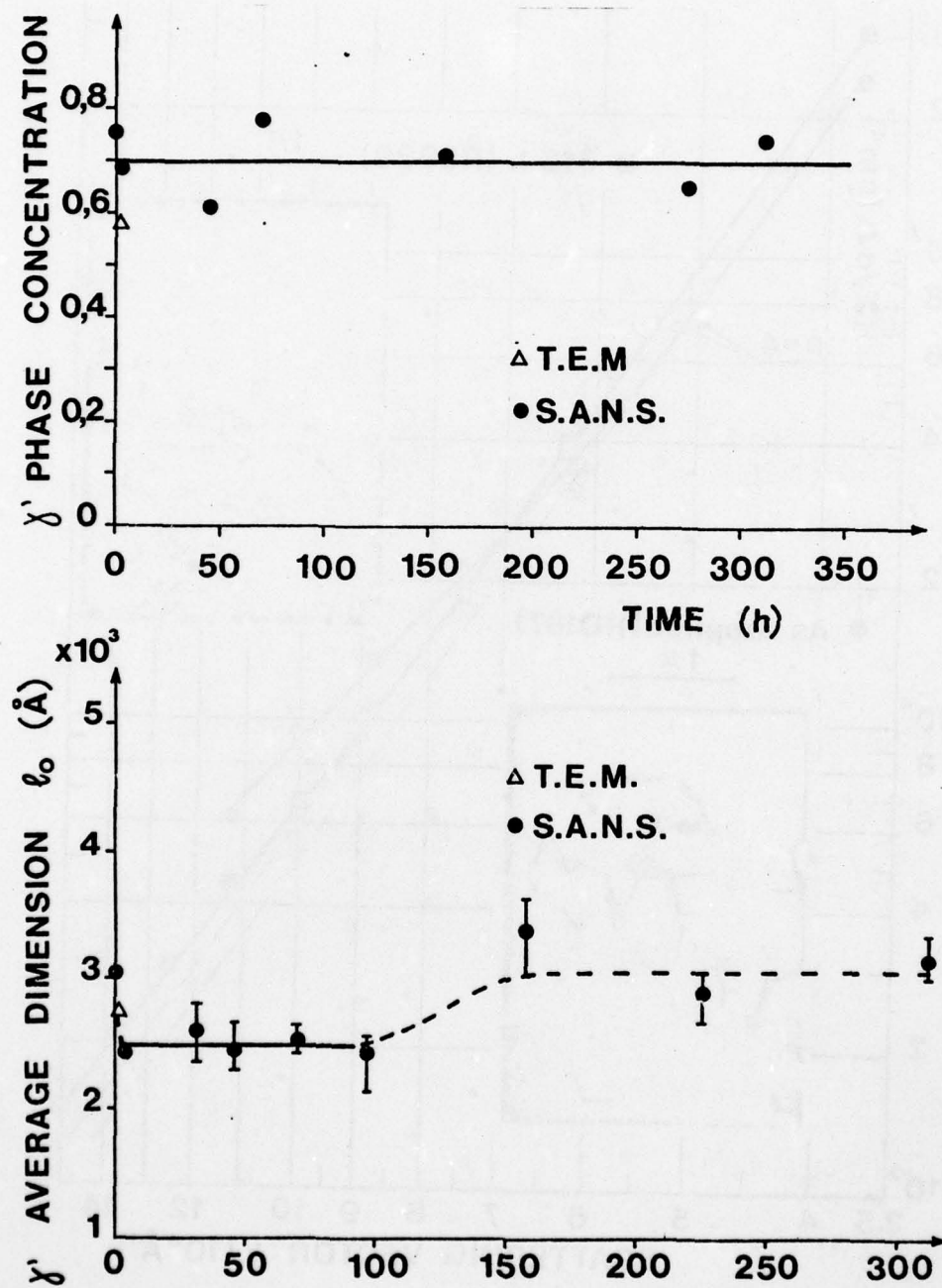


Fig. 30 IN-100 turbine blades. Size and density of γ' as a function of aging time (FIAT).

versus time for both methods. Again, agreement with TEM measurements is most gratifying.

iii. INCOLOY - 800

This austenitic steel contains the maximum amount of Ni. Three specimens of this alloy were heat treated. Table IX gives the alloy compositions and the heat treatment schedules. Fig. 31 shows the scattering curves and TEM photos for specimens, as-received and subject to a creep load of 37 Nw/mm^2 at 700°C for over 5000 hours. The SANS results show an overall increased intensity, but no region that shows clear linearity (i.e., no Guinier region). There is obviously a large size distribution, which must be analyzed by standard methods. There is good agreement between an average SANS-determined size and that found with TEM; $\sim 1300 \text{ \AA}$.

A Porod analysis has been carried out on this data; Eq. (15), and a correlation length has been determined as a function of time; Fig. 32. For the creep specimen the correlation length is a measure of the average dimension of the creep-induced voids. Such studies have actually just begun; there is clearly much to do.

iv. INCOLOY - 700

This superalloy is strengthened by the distribution of the γ' phase. As the γ' grows, in-service, due to thermally-induced coarsening as well as mechanical effects, the alloy weakens until it becomes ineffective in service and must be either re-heat treated or discarded. It is possible to use SANS to follow the evolution of γ' , and, thus, to determine the mechanical condition of the alloy.

TABLE IX

INCOLOY 800 (Grade 2 ASTM)	COMPOSITION (%)											HEAT TREATMENT	ASTM GRAIN SIZE	
	C	Si	Mn	Cr	Ni	Ti	Al	Fe	S	P	Others			Ti+Al
Material A	0.044	0.55	0.54	22.1	33.5	0.31	0.21	Bal	0.004	0.010	0.026	0.52	5min 1140°C WQ	5.5
" B	0.044	0.65	0.59	21.0	31.5	0.45	0.41	Bal	0.004	0.012		0.86	20min 1150°C WQ	3.5 - 5
" C	0.039	-	-	21.1	32.0	0.45	0.21	Bal	-	-		0.66	1 h 1150°C	2 - 6

ALLOY 800 - CREEP

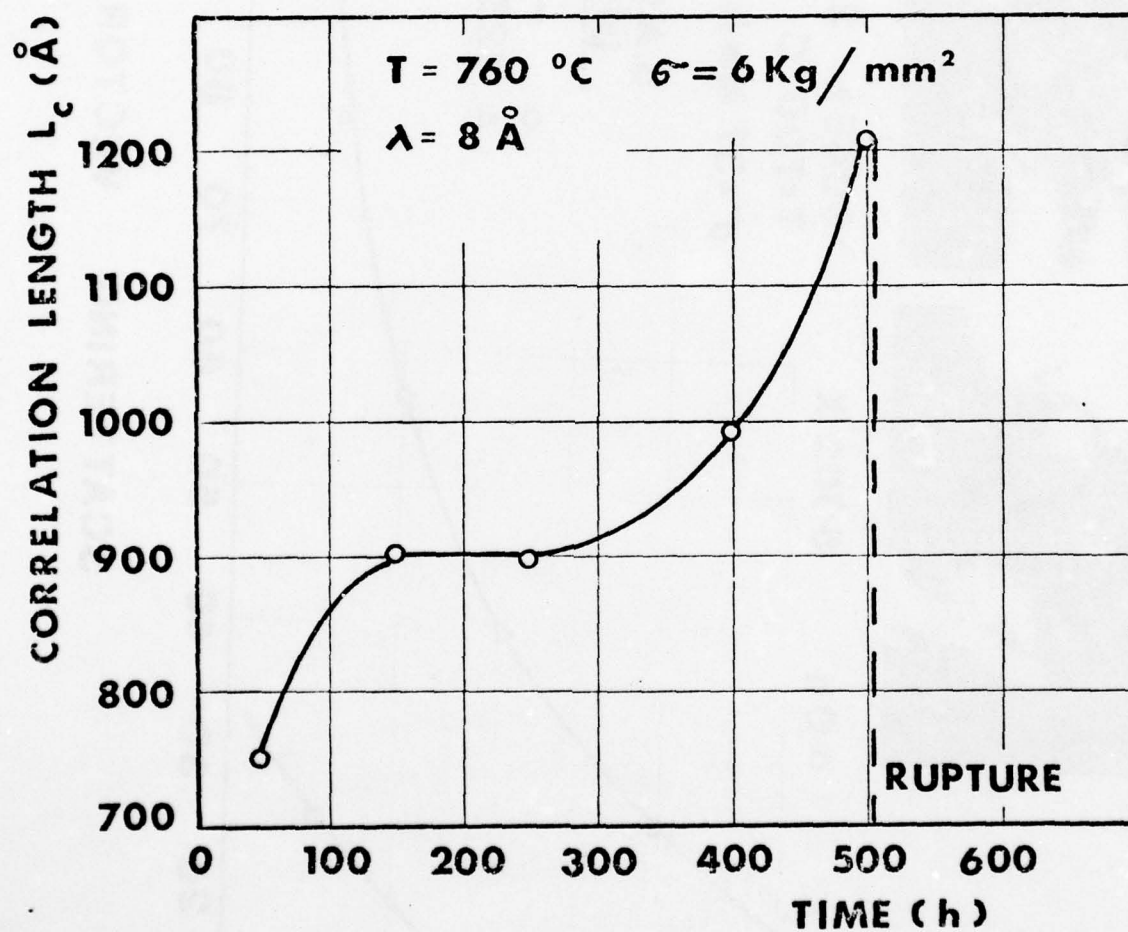


Fig. 32

Correlation length during creep of Alloy 800 at 760°C loaded as-indicated (FIAT).